J. Fluid Mech. (1997), *vol.* 348, *pp.* 29–83. Printed in the United Kingdom

Investigation of transition to turbulence using white-noise excitation and local analysis techniques

By F. N. SHAIKH†

Engineering Department, Queen Mary and Westfield College, Mile End Road, London E1 4NS, UK

(Received 14 June 1995 and in revised form 22 May 1997)

Weak free-stream turbulence excites modulated Tollmien–Schlichting (T–S) waves in a laminar boundary layer that grow in magnitude with downstream distance and ultimately lead to the formation of turbulent spots and then fully turbulent flow. Hot-wire experiments have indicated that the development of localized large-amplitude 'events' in the velocity records are the essential precursor to the eventual formation of turbulent spots in the flow field. Traditional global Fourier techniques are unable to resolve the localized nature of these events and hence provide little useful information concerning the physical processes responsible for this breakdown process.

This investigation used sequences of computer-generated deterministic white noise to excite a laminar boundary layer via a loudspeaker embedded in a flat-plate model. This form of excitation generated the modulated disturbance waves of interest a short distance downstream from the source in a repeatable and deterministic manner. Further downstream the pattern of flow breakdown and subsequent generation of turbulent spots was similar to that observed in naturally excited situations. By repeatedly exciting the boundary layer with a single white-noise sequence it was possible to examine the highly nonlinear stages of 'event' development and breakdown with a single hot-wire probe.

Two local analysis techniques, the wavelet transform (WT) and singular spectrum analysis (SSA), were used in conjunction with the white-noise excitation technique to examine the highly nonlinear flow mechanisms responsible for the localized formation of events that lead to the eventual breakdown to turbulence.

1. Introduction

1.1. *Background*

The exact route to turbulence observed in a transitional flat-plate boundary layer is dependent on the magnitude and form of the external excitation. The boundary layer receptivity governs the mechanism by which the background environment generates boundary layer disturbances. In general, large excitation leads directly to turbulent flow through some 'bypass' mechanism, whereas lower levels of excitation excite vorticity waves that grow in magnitude with downstream distance, leading to turbulence by a more gradual route. Observations from flight and wind tunnel experiments have indicated that the transition process in this latter case can be divided into three distinct stages:

(i) the boundary layer acts as a linear filter amplifying a select spectral band of disturbances;

† Present address: Rover Group Ltd, Gaydon Test Centre, Banbury Road, Lighthorne, Warwick CV35 0RG, UK.

(ii) the finite-amplitude disturbances interact nonlinearly and modify the base flow;

(iii) the unsteady base flow then leads to the birth and growth of turbulent spots that coalesce and develop into a fully turbulent boundary layer.

Stage (i) is usually described as a linear instability of the laminar base flow that leads to the growth of disturbances. Boundary layer flows are 'open systems' and behave quite differently from 'closed systems' such as Taylor–Couette flow between concentric rotating cylinders. Closed systems describe flows that are confined by boundaries and uncoupled to external disturbances. The linear stability of these flows is generally governed by a single parameter and once a critical value of this parameter is exceeded initially infinitesimally small disturbances grow exponentially in time until nonlinear effects moderate the process. These flow fields, therefore, are temporally unstable and require no external excitation.

Boundary layers, on the other hand, are not completely confined and require excitation from external sources. The latter excite weak perturbations in the base flow that evolve as vorticity waves (Tollmien–Schlichting waves) that amplify or decay with downstream distance. The waves are generated by external factors and arise therefore as forced oscillations rather than through naturally occurring instabilities. The growth rate of the disturbances is dependent on the Reynolds number and their frequency content. Once a critical Reynolds number has been exceeded, a portion of the disturbance spectrum amplifies with downstream distance until the effects of nonlinearity modify the process.

Schubauer & Skramstad (1948) provided the first experimental evidence supporting the stability viewpoint of boundary layer transition. S & S reduced the background disturbances of their wind tunnel to a low level and initially examined the 'natural' transition of a flat-plate boundary layer using hot-wire anemometry. Their measurements indicated that the resulting boundary layer disturbances were initially almost sinusoidal in form but contained a slow amplitude modulation. These disturbances grew in amplitude and became less sinusoidal with downstream distance, until the hot-wire records showed evidence of the formation of turbulent spots. Schubauer & Skramstad (1948) then used a surface-mounted vibrating ribbon to excite the boundary layer with a two-dimensional regular periodic disturbance in order to examine the early stage of the observed transition process in greater detail. They concluded that the previously identified sinusoidal velocity fluctuations were linked to the Tollmien–Schlichting (T–S) waves predicted by linear stability analysis.

The majority of the subsequent investigations into the second nonlinear stage of the transition process have continued to use this type of artificial excitation. These studies have identified a rich variety of nonlinear phenomena and have lead to significant advances in our understanding of transition. A full discussion of the results of these investigations is given by Kachanov (1994). However, during this stage of the transition process the boundary layer can be viewed as a forced nonlinear system and as such is extremely sensitive to input conditions; thus a wide range of nonlinear phenomena can be observed by relatively small changes in the nature of the input excitation. Thus it is not clear whether investigations using artificial harmonic excitation capture the essential nonlinear processes observed in flows excited by the weak free-stream turbulence observed in flight, Mullender & Poll (1995).

In contrast, Gaster & Grant (1975) used a short-duration acoustic pulse to excite a wavepacket in a flat-plate boundary layer. Gaster (1978, 1981) noted significant nonlinear effects in the behaviour of the wavepacket even though the peak-to-peak amplitudes of the hot-wire records were well below levels for which nonlinear effects were to be expected for purely periodic waves. Gaster (1981) concluded that the

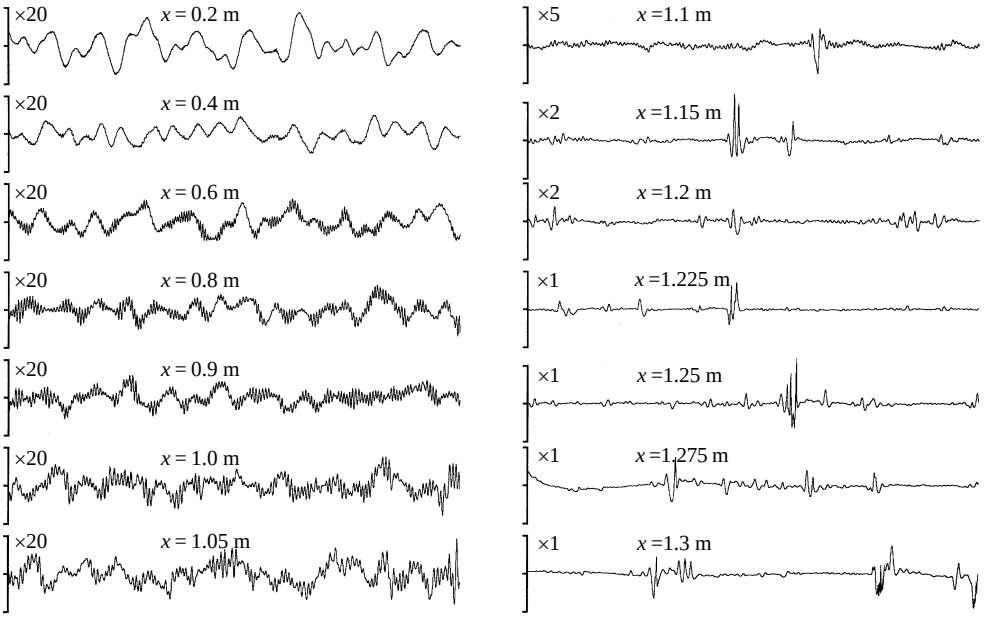

FIGURE 1. Evolution of the velocity records with downstream distance at $\eta = 0.65$ ($\eta = y(U/2\nu x)^{1/2}$) from the free-steam excited experiment of Shaikh (1997). Time duration = 0.41 s. Velocities are plotted as $u'/U\,\%$, and scaled individually. Vertical scales are given as factors of magnification of the scale associated with $x = 1.3$ m that has an absolute value of $\pm 20\,\%$.

modulation of the wavetrains resulted in nonlinear mechanisms that were not apparent with regular periodic waves and thus were responsible for the difference in the evolution of the respective disturbance systems. It appeared, therefore, that the modulation of the wavetrains may play an important role in the nonlinear development of the initial disturbance system observed in naturally excited transition where the wavetrains are modulated. Consequently, Gaster (1978, 1993) suggested using computer-generated deterministic white noise as an alternative form of artificial excitation that was more relevant to the development of such flows.

The author used this technique in a number of investigations that examined the nonlinear development of modulated disturbances and the subsequent breakdown of the flow leading to the formation of turbulent spots. The characteristics of boundary layers with significant levels of intermittency were also studied. During the course of this work it became clear that traditional global Fourier techniques were not able to resolve the localized nature of large-amplitude regions of the velocity records found in these experiments. Two localized analysis techniques, the wavelet transform (WT) and singular spectrum analysis (SSA), were therefore developed and used to analyse the experimental data.

The white-noise technique generates amplitude-modulated T–S disturbances that evolve spatially and break down to turbulent spots in a deterministic manner in the sense that the spatial location of a spot is fixed for a particular noise series. The work presented here used the WT and SSA to examine hot-wire records obtained from three experiments that used sequences of computer-generated white noise to excite a flat-plate boundary layer. The first experiment examined the three-dimensional flow field associated with a localized coherent flow structure that was identified as the precursor to a turbulent spot, the second experiment used the WT to examine the breakdown of

Station	1	2	3	4	5	6	7
Distance (m)	0.2	0.4	0.6	0.8	0.9	1.0	1.05
$Re_x \times 10^{-6}$	0.393	0.786	1.179	1.572	1.769	1.975	2.064
Station	8	9	10	11	12	13	14
Distance (m)	1.10	1.15	1.20	1.225	1.250	1.275	1.30
$Re_x \times 10^{-6}$	2.162	2.26	2.358	2.407	2.457	2.506	2.555

TABLE 1. Positions and associated Reynolds numbers of streamwise measurement stations used in the free-steam excited experiment

this structure and the generation of high-frequency disturbances that preceded the formation of a spot, whilst the third experiments used SSA to study the 'natural' formation and subsequent streamwise development of spots.

Selected results from the investigation into the final stage of transition were presented previously in Shaikh & Gaster (1994*b*) and in two brief conference proceedings, Shaikh & Gaster (1993, 1994*a*). The aim here is to discuss the development and use of the two local analysis techniques in greater detail and, in addition, to use the techniques in conjunction with white-noise excitation to present an overall view of the transition process.

The work described here is a continuation of Shaikh (1997) that compared the overall pattern of white-noise-excited transition with that excited by weak free-stream turbulence. The following subsection, §1.2, briefly describes the relevant results from this work and §1.3 discusses the requirement for local analysis techniques.

1.2. *White-noise excitation*

Shaikh (1997) initially re-examined the pattern of transition observed in a boundary layer excited by weak free-stream turbulence. Figure 1 shows a number of fluctuating streamwise velocity records obtained from consecutive streamwise measurement stations in this naturally excited experiment. Table 1 lists the streamwise locations and associated Reynolds numbers of the measurement stations: the signals were obtained at a constant non-dimensional distance from the wall given by $\eta = 0.65$, where

$$\eta = y\left(\frac{U}{2\nu x}\right)^{1/2},$$

and the time duration is 0.41 s. The velocity records are plotted as a percentage of the free-stream velocity ($u'/U\,\%$, $U = 30\ \mathrm{m\ s^{-1}}$) and scaled individually for convenience. The vertical scales are given as factors of magnification of the scale $\pm 20\,\%$.

The figure shows that the naturally excited waves exhibited a broad-band character. The time series from the most upstream measurement station is characterized by irregular flow-frequency oscillation typical of this region of the flow field. Kendall (1985, 1990) and Westin *et al.* (1995) suggested that these low-frequency fluctuations are caused by longitudinal streaky structures that are linked to the receptivity of the boundary layer and originate from the leading edge of the plate. At the low levels of free-stream excitation under consideration, less than 0.03 %, these disturbances decayed with downstream distance and it is not clear what role if any these structures play in the overall transition process observed in this experiment.

Slightly further downstream figure 1 shows that a second higher frequency oscillation develops superimposed on the original irregular signal. A close examination of these latter oscillations revealed a waveform modulated in amplitude containing

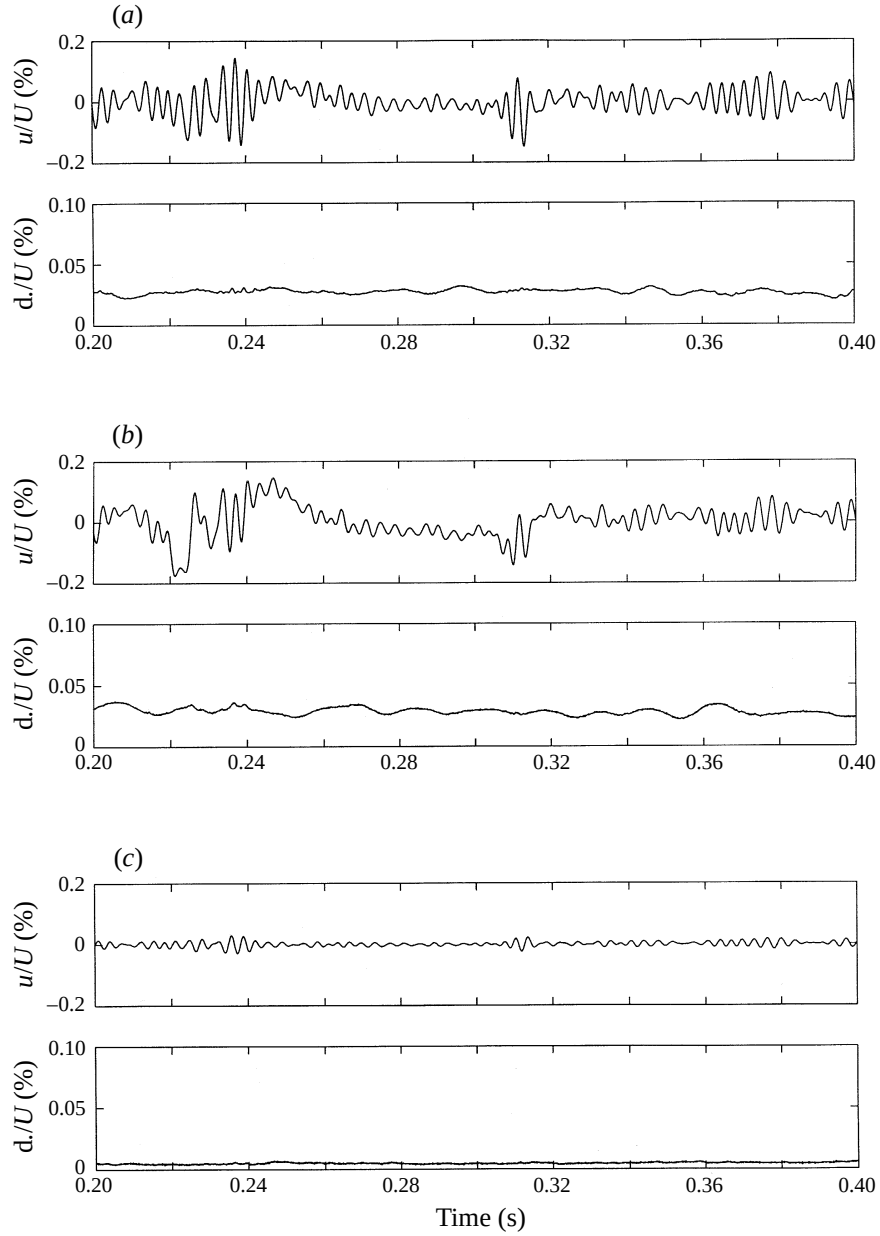

FIGURE 2. Ensemble-averaged velocity record and associated standard deviation measured at three non-dimensional wall locations at $x = 0.4$ m: (*a*) $\eta = 0.35$; (*b*) $\eta = 1.1$; (*c*) $\eta = 4.24$. Results from the white-noise experiment of Shaikh (1997).

packets of T–S waves caused by the selective amplification of certain frequency bands. The spectral composition of these disturbances initially developed in a manner consistent with predictions from linear stability analysis. Further downstream, however, the flow field was characterized by isolated departures from the linear pattern. These excursions or 'events' grew rapidly in amplitude with streamwise distance and eventually exhibited bursts of high-frequency oscillations. This pattern of behaviour is evident in the velocity record corresponding to $x = 1.3$ m which shows a high-

frequency 'burst' superimposed on an event. This portion of the signal is indicative of the passage of an incipient turbulent spot over the hot-wire probe. Shaikh (1997) suggested that the observed pattern of localized flow breakdown and the formation of turbulent spots is quite different from that observed during the final stages of harmonically excited transition, and that modulated waves evolve quite differently from their harmonically excited counterparts when the disturbance amplitudes are large enough for nonlinear effects to be significant.

Figure 2 shows a number of time series obtained in a second experiment using computer-generated white-noise excitation via a loudspeaker embedded in a flat plate. The boundary layer was excited 40 times by the same deterministic white-noise series and hot-wire anemometry was used to measure the response at stations distributed through the boundary layer at a number of streamwise locations that are listed in table 2. The response was ensemble averaged to generate a spatio-temporal picture of the evolution of the disturbance flow. The free-stream velocity for this experiment was set at 18 m s^{-1}.

Figure 2(*a*) shows two time series from the most upstream measurement station, $x = 0.4$ m, at a non-dimensional wall position given by $\eta = 0.35$. The upper trace is the ensemble average of the 40 realizations obtained at this station whilst the lower trace gives a measure of the standard deviation. The averaged signal shows amplitude-modulated oscillations that correspond to T–S disturbances in the flow. The relatively low value of the standard deviation indicates that the response of the boundary layer to the white-noise excitation is essentially deterministic and repeatable at this location. Figures 2(*b*) and 2(*c*) show similar traces from non-dimensional wall positions given by $\eta = 1.1$ and $\eta = 4.24$ respectively. It is clear that, downstream of the source, the white-noise technique generated the modulated disturbances of interest in a repeatable and deterministic manner.

Shaikh (1997) followed the evolution of this disturbance system and demonstrated that white-noise excitation generated amplitude-modulated T–S waves that break down to turbulence in a manner similar to naturally excited waves. Figure 3 shows time series obtained at $\eta = 1.1$ from consecutive streamwise measurement stations. Once again the time series from the upstream station, $x = 0.4$ m, show modulated deterministic T–S disturbances. The spectral composition of these disturbances and their initial downstream development compared favourably with predictions from two-dimensional stability analysis. The modulated T–S signals are still evident 300 mm further downstream in figure 3(*b*); however, the figure also shows the development of a compact localized event near the centre of the record. Although the standard deviation increases marginally in the neighbourhood of the event, the flow field is still essentially repeatable.

The magnitude of the event has increased by a factor of twenty at $x = 0.975$ m in figure 3(*c*), and in addition two other events can be seen at the extreme ends of the averaged velocity record. The remainder of the signal is still composed of amplitude-modulated oscillations, but of a much smaller amplitude and so are not apparent at this scale. The standard deviation associated with the event shows a dramatic increase in magnitude at this spatial location indicating that whilst the remainder of the signal is essentially repeatable, the signature of the event shows sample-to-sample variation. A close examination of the standard deviation reveals a slight 'crinkling' of the peak in the neighbourhood of the event, presumably caused by the occurrence of random bursts of high-frequency oscillations in the individual velocity records. Figure 4 shows part of a single realization of the velocity record obtained at $\eta = 4.24$ that clearly shows a high-frequency wavepacket superimposed on a signal consisting of amplitude-

Station	1	2	3	4	5	6
Distance (m)	0.4	0.6	0.7	0.8	0.9	0.95
$Re_x \times 10^{-6}$	0.243	0.485	0.728	0.97	1.091	1.213
Station	7	8	9	10	11	12
Distance (m)	0.96	0.965	0.975	1.0	1.05	1.1
$Re_x \times 10^{-6}$	1.273	1.334	1.394	1.455	1.485	1.516

TABLE 2. Positions and associated Reynolds numbers of streamwise measurement stations used in the artificially excited experiment

modulated T–S disturbances. The frequency of the wavepacket appears to be approximately five times that of the background T–S frequency. Finally figure 3(*d*) at $x = 1.1$ m shows that two of the events identified in the previous time series have developed into fully turbulent spots.

Shaikh (1997) concluded that the white-noise excitation was a powerful technique that permitted the entire development of amplitude-modulated T–S disturbances to be examined in a controlled manner. The technique could also be used as an alternative means of generating turbulent spots when studying the latter intermittency-dominated stage of transition. The highly localized nature of the nonlinear development of the disturbance system, however, posed a number of problems when traditional signal analysis techniques were used to examine the flow mechanisms involved in more detail.

1.3. *Local analysis techniques*

Figure 5 shows the power spectra of four of the velocity records given in figure 1. The figure indicates that that appearance and development of the events in the hot-wire records were associated with a gradual broadening and 'filling' of the power spectra. It is clear that traditional global Fourier decomposition was not able to resolve the localized nature of the large-amplitude regions of the velocity records and so resulted in full power spectra. This technique cannot therefore provide useful information concerning the development, growth and breakdown of these localized structures.

The Fourier transform decomposes a signal onto a set of orthogonal trigonometric basis functions, the signal being represented by a linear combination of these Fourier vectors. The basis functions are of an infinite extent and therefore localized information in the signal is distributed over the entire frequency axis. Thus a localized 'event' in a velocity record nominally composed of low-amplitude oscillations makes a contribution to each of the complex Fourier coefficients and results in a full power spectrum. Any subsequent Fourier plane filtering of the signal produces ambiguous results as the singularity in the time series contaminates the entire Fourier plane.

The analysis of time series that contain localized information requires the use of local analysis techniques that prevent global contamination by singularities. The majority of these strategies satisfy this requirement by either using basis functions that are simultaneously compact in the space and frequency domains, or by analysing the signal as it appears when viewed through a set of identical windows, smaller than the original signal, that are translated with respect to each other. The WT and SSA are examples of two such local analysis techniques: the WT projects the signal to be analysed onto a family of compact basis functions whilst SSA views the signal through translated windows.

The WT was used to examine the breakdown of the flow field associated with an 'event' in the velocity records and to characterize the subsequent development of a

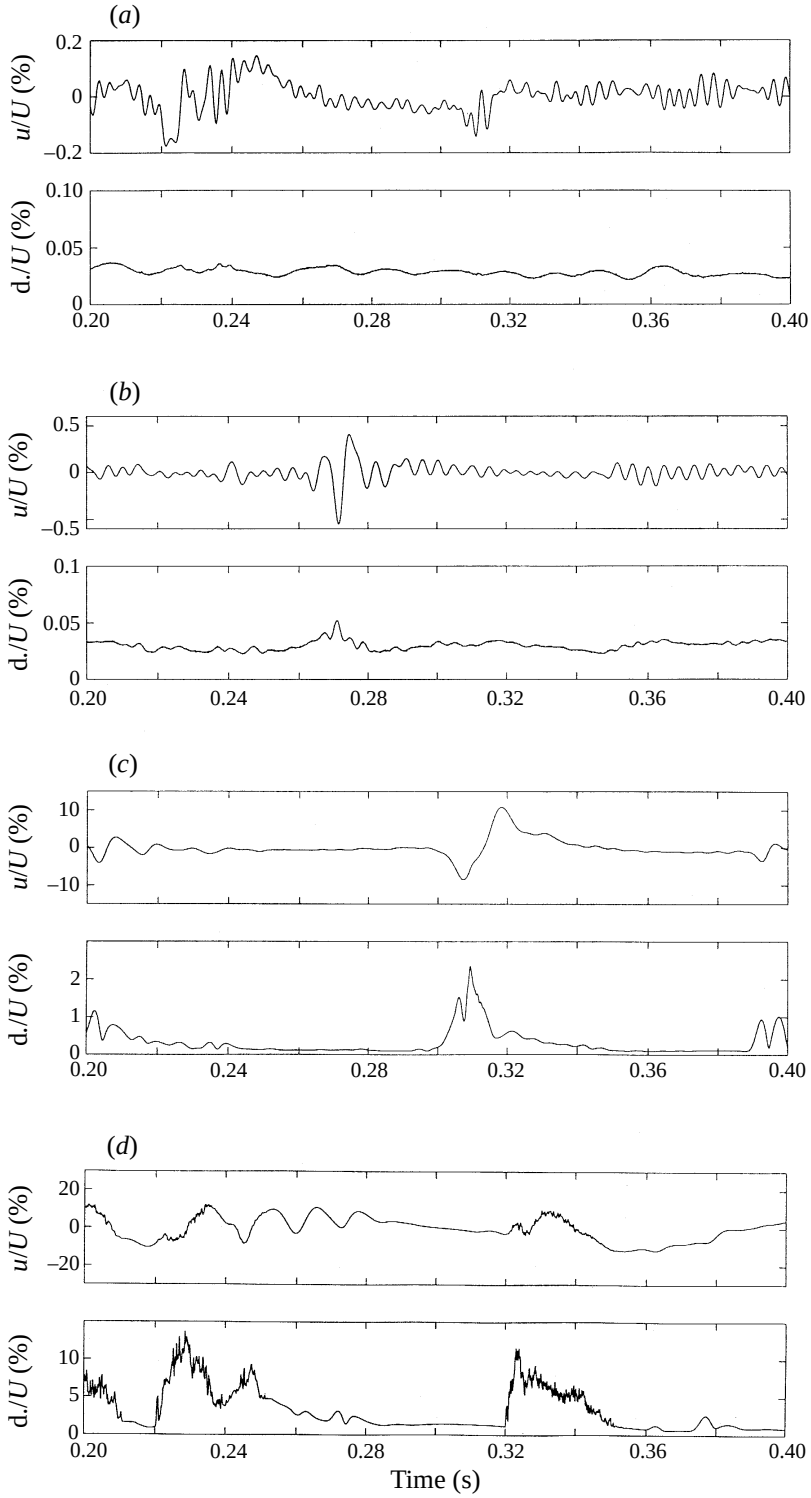

FIGURE 3. Ensemble-averaged velocity record and associated standard deviation measure at a constant non-dimensional height, $\eta = 1.1$, from consecutive streamwise measurement stations: (*a*) x = 0.4 m; (*b*) $x = 0.7$ m; (*c*) $x = 0.975$ m; (*d*) $x = 1.1$ m. Results from the white-noise experiment of Shaikh (1997).

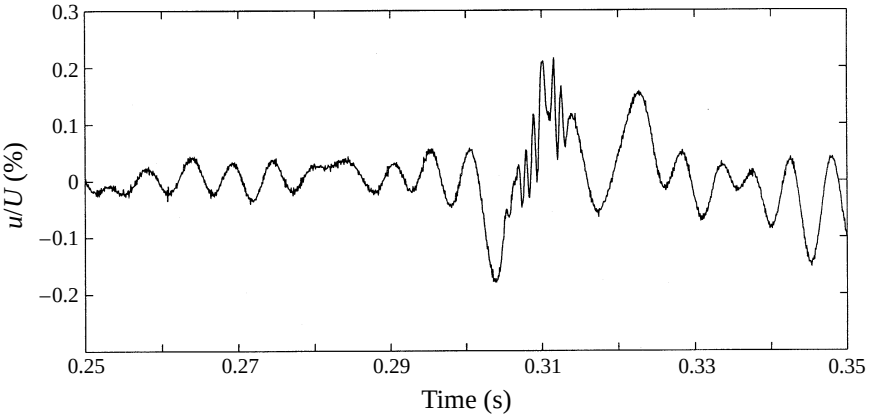

FIGURE 4. Single realization of a fluctuating velocity record showing a high-frequency burst at $x = 0.975$ m $\eta = 4.24$. Results from the white-noise experiment of Shaikh (1997).

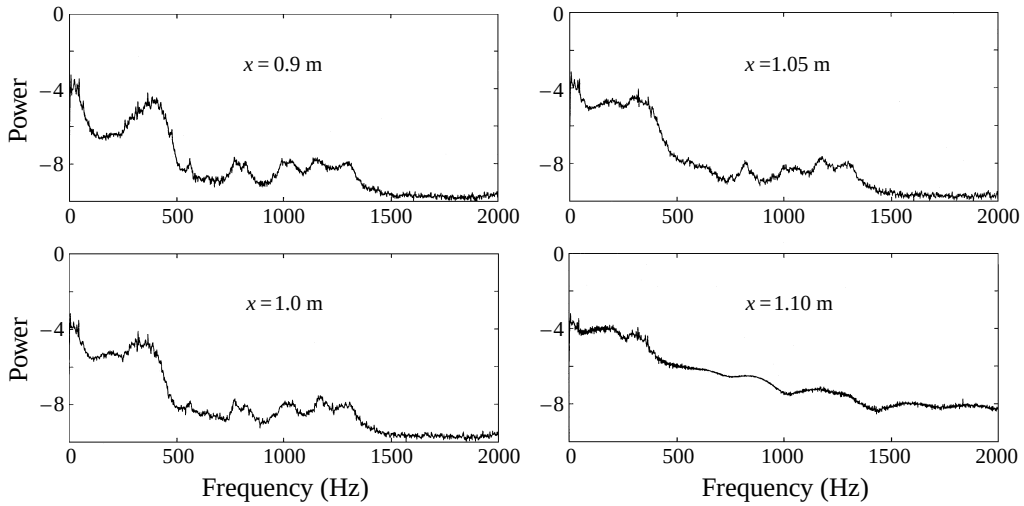

FIGURE 5. Power spectra associated with four consecutive downstream measurement stations plotted on a log-linear scale (velocity records given in figure 1). Results from the free-stream excited experiment of Shaikh (1997).

turbulent spot. The intermittency parameter, the proportion of time that the boundary layer is turbulent, is usually used to characterize the state of the boundary layer during this final stage of transition. The majority of intermittency measurement techniques suffer from a degree of ambiguity due to the requirement for a number of arbitrary threshold criteria. SSA was used to provide a very simple method for the automatic detection of spots in a velocity record and also to give a measure of the signal intermittency based upon a single physically meaningful threshold criterion.

2. The wavelet transform

2.1. *Background*

Gabor (1946) was the first to suggest that the time-frequency description of a signal could be obtained by the Fourier analysis of the signal as it appeared when viewed through identical windows that were translated with respect to each other. Gaussian

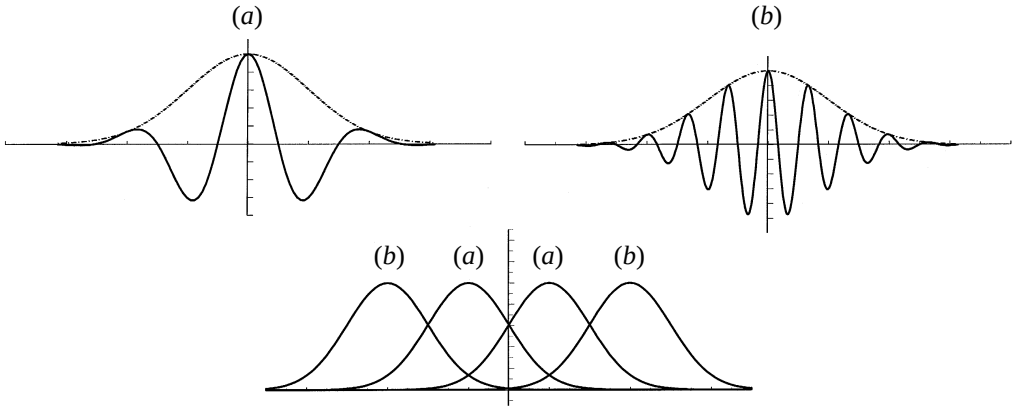

FIGURE 6. (*a*) Time-domain representation of two typical basis functions used in the Gabor transform. (*b*) Frequency-domain characteristics of the two basis functions.

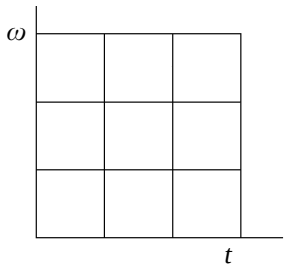

FIGURE 7. Diagram showing the fixed resolution of the Gabor Transform in the time–frequency plane.

windows were used initially as they were simultaneously well localized in the time and frequency domains. The Gabor transform, therefore, projected a signal onto a set of basis functions that were complex exponentials with Gaussian envelopes. The time–frequency plane was generated by the repeated convolution of the raw signal with trigonometric functions of increasing frequency in windows of constant size. Figure 6 shows the time and frequency plane representations of the basis functions used in the Gabor transform.

The Gabor transform is an example of a short-time Fourier transform (STFT); other methods within this class use different windowing functions and hence have subtly different characteristics in the time–frequency plane. However, all STFT have the property that the band width and time duration of the analysing functions are constant and independent of the centre frequency. Thus the resolution of this technique in the time–frequency plane is fixed and independent of the centre frequency of the analysing functions, as shown in figure 7.

Morlet (1981) (see Farge 1992) suggested the WT as an alternative to the STFT. The wavelet approach decomposes a signal onto a set of basis functions that have a constant band-width to centre-frequency ratio. The basis functions are generated by the translations and dilations of a single 'mother' function that is localized simultaneously in the space (or time in some instances) and frequency domains. The analysing functions or 'wavelets', therefore, are scaled versions of the mother function in that they have the same shape as the original function but varying time durations or 'scales'.

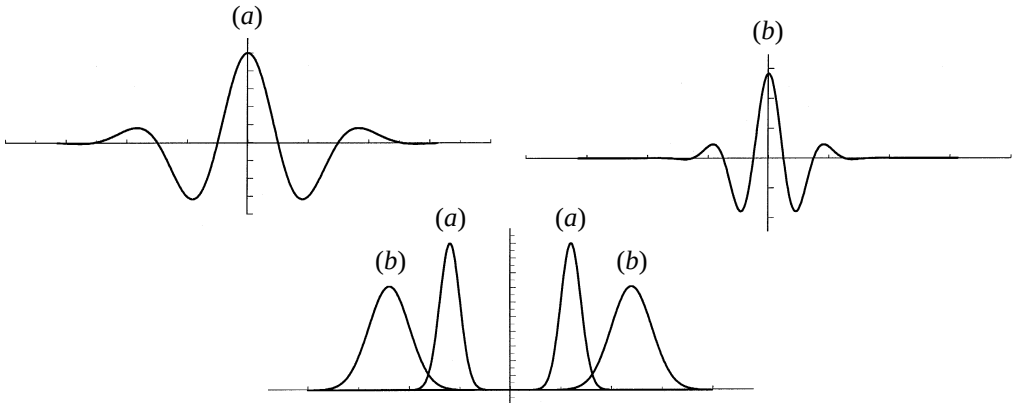

FIGURE 8. (*a*) Time-domain representation of two typical basis functions used in the wavelet transform. (*b*) Frequency-domain characteristics of the two basis functions.

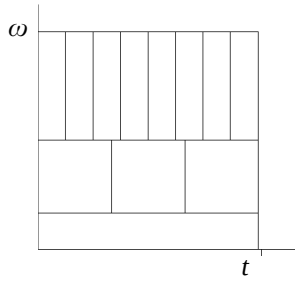

FIGURE 9.Diagram showing the varying resolution of the wavelet transform in the time–frequency plane.

The WT maps a one-dimensional signal on to a two-dimensional time-scale or 'wavelet' plane by the repeated convolution of the signal with wavelets of varying scales. As the time duration or scale of the wavelet decreases for a constant function shape, the centre frequency of the scaled function increases relative to that of the original mother function, the converse being true for wavelets of increasing relative scales. Figure 8 shows the time and frequency plane representations of the wavelet basis functions. The wavelet approach differs from that of the STFT in that the WT substitutes the frequency scaling of the STFT for a scaling based on the scale or time duration of the wavelet functions, this difference is clear in a comparison of figures 6 and 8.

Each member of the family of scaled wavelets can be considered to be the impulse response of a band-pass filter in which the centre frequency and the band width of the filter vary with the scale of the analysing wavelet. This property of the WT implies that, unlike the STFT, the resolution of the WT (figure 9) varies with the scale of the analysing wavelet as shown by a comparison of figures 7 and 9. The WT, therefore, analyses a signal at a number of scales, permitting both the global and local properties of a signal to be represented simultaneously.

Since its introduction the WT has been used in a number of different fields: Farge (1992), Rioul & Flandrin (1992) and Combes, Grossman & Tchamitchian (1989) provide comprehensive derivations of the wavelet transform and describe a number of applications. The following subsections review the formulation of the WT and discuss the application of the technique to the analysis of flows containing localized events.

2.2. *Implementation and properties*

The WT at a scale s is generated by the projection of the real signal $f(x)$ onto the scaled wavelet $\sigma_s(x)$ given by

$$\sigma_s(x) = s^{1/2}\sigma(sx),$$

where $\sigma(x)$ is the original analysing or mother wavelet. The projection is the inner product of the signal with a set of wavelets generated by shifting or translating the scaled wavelet. The shift operator $\sigma_u(x)$ for the translation parameter u is given by

$$\sigma_u(x) = \sigma(x-u).$$

Thus the continuous wavelet transform $\psi(s,u)$ of the signal $f(x)$ is

$$\psi(s,u) = \int_{-\infty}^{\infty} f(x)\, s^{1/2}\sigma(s(x-u))\,\mathrm{d}x. \tag{1}$$

In order to reconstruct the original signal, the Fourier transform of the analysing wavelet, $\hat{\sigma}(\omega)$, must satisfy the admissibility condition

$$C_\sigma = \int_0^{\infty} \frac{|\hat{\sigma}(\omega)|^2}{\omega}\mathrm{d}\omega < \infty, \tag{2}$$

then

$$f(x) = \frac{1}{C_\sigma}\int_{-\infty}^{\infty}\int_0^{\infty} \psi(s,u)\,\sigma_s(x-u)\,\mathrm{d}s\,\mathrm{d}u. \tag{3}$$

The admissibility condition (2) implies that $\hat{\sigma}(0) = 0$ (the wavelets have zero mean) and that $\hat{\sigma}(\omega)$ is small near $\omega = 0$.

By writing $\tilde{\sigma}_s(x) = \sigma_s(-x)$, the WT can be written as a convolution product,

$$\psi(s,u) = f(x) * \tilde{\sigma}_s(u), \tag{4}$$

indicating that the WT can be viewed as the repeated action of a family of band-pass filters with impulse response $\hat{\tilde{\sigma}}_s(\omega)$. Thus instead of integrating (1) directly, the wavelet transform of a signal can be generated more efficiently by evaluating the convolution product (4) in the Fourier plane using fast Fourier transforms (FFT). However, this implementation imposes restrictions on the upper and lower bounds of the scale parameter. The lower bound is imposed by ensuring that the small-scale high-frequency wavelet filters do not extent beyond the Nyquist limit in the frequency plane, whereas the upper bound is set by preventing the large-scale low-frequency wavelet filters from ringing due to the relatively sharp filter cut-off.

The wavelet coefficients generated using a real analysing function contain both phase and magnitude information. These contributions to the wavelet coefficients can be separated by using a complex or progressive wavelet that satisfies the condition

$$\hat{\sigma}(\omega) = 0 \,\forall\, \omega < 0.$$

The magnitude information is usually displayed on a plane spanned by time t and $-\log s$. The localized nature of the analysing wavelet in the time domain ensures that local signal information is not transmitted to the entire wavelet plane. Figure 10(*a*) shows that a point u_0 in the signal influences a limited region of the wavelet plane. At small values of $-\log s$ the analysing wavelet is highly resolved in time and thus information

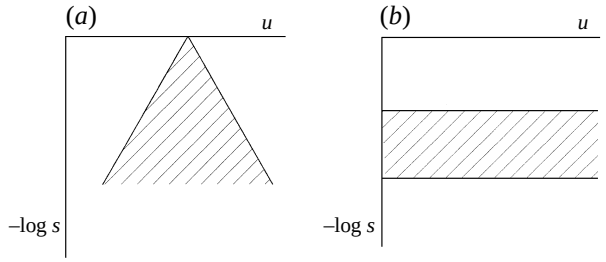

FIGURE 10. (*a*) Space (or time)-domain and (*b*) frequency domain influence regions of the wavelet transform.

is retained locally; at larger values, however, the time resolution deteriorates and the information is transmitted to a larger region of the transform plane. In addition, figure 10(*b*) shows that the Fourier component, $\hat{f}(\omega)$, has a complementary region of influence described by a rectangular strip in the wavelet plane.

2.3. *Choice of analysing wavelet*

The velocity records obtained from the latter stages of the white-noise-excited flow field indicated that the development and breakdown of large-amplitude localized events immediately preceded the appearance of turbulent spots in the flow. The wavelet transform is the ideal tool to use when attempting to analyse and characterize this localized breakdown process. However, the wavelet plane generated by a particular analysing function contains information from both the signal and the wavelet, thus different wavelets highlight different aspects of the signal. The form of the wavelet used in a particular application is therefore dependent on the signal information required.

The Morlet wavelet, shown in figure 11(*a*), is the most commonly used progressive wavelet and is generated from a plane wave with a Gaussian envelope,

$$\sigma(x) = \exp[-|x|^2/2 + \mathrm{i}mx],$$

and

$$\hat{\sigma}(\omega) = (2\pi)^{1/2}\exp[-(m-\omega)^2/2], \quad \omega > 0$$
$$\hat{\sigma}(\omega) = 0, \quad \omega \leqslant 0.$$

However, the wavelet is admissible for $m > 5.5$ only. The following modification ensures that the wavelet is unconditionally admissible:

$$\hat{\sigma}(\omega) = (2\pi)^{1/2}\omega^{1/4}\exp[-(m-\omega)^2/2], \quad \omega > 0$$
$$\hat{\sigma}(\omega) = 0, \quad \omega \leqslant 0.$$

The time-domain representation of the modified Morlet wavelet is given in figure 11(*b*). The Paul wavelet (Farge 1992) shown in figure 11(*c*) is another commonly used progressive wavelet, where

$$\sigma_m(x) = \frac{\Gamma(m+\mathrm{i})\,\mathrm{i}^m}{(1-\mathrm{i}x)^{1+m}},$$

and

$$\hat{\sigma}_m(\omega) = \omega^m e^{-\omega}, \quad \omega > 0$$
$$\hat{\sigma}_m(\omega) = 0, \quad \omega \leqslant 0.$$

Real-valued functions have also been used in the wavelet analysis of signals. The most common wavelets of this type and derivatives of the Gaussian distribution,

$$\sigma_m(x) = (-1)^m \frac{\mathrm{d}^m}{\mathrm{d}x^m}(\exp[-|x|^2/2]),$$

$$\hat{\sigma}_m(\omega) = m(\mathrm{i}\omega)^m \exp[-|\omega|^2/2].$$

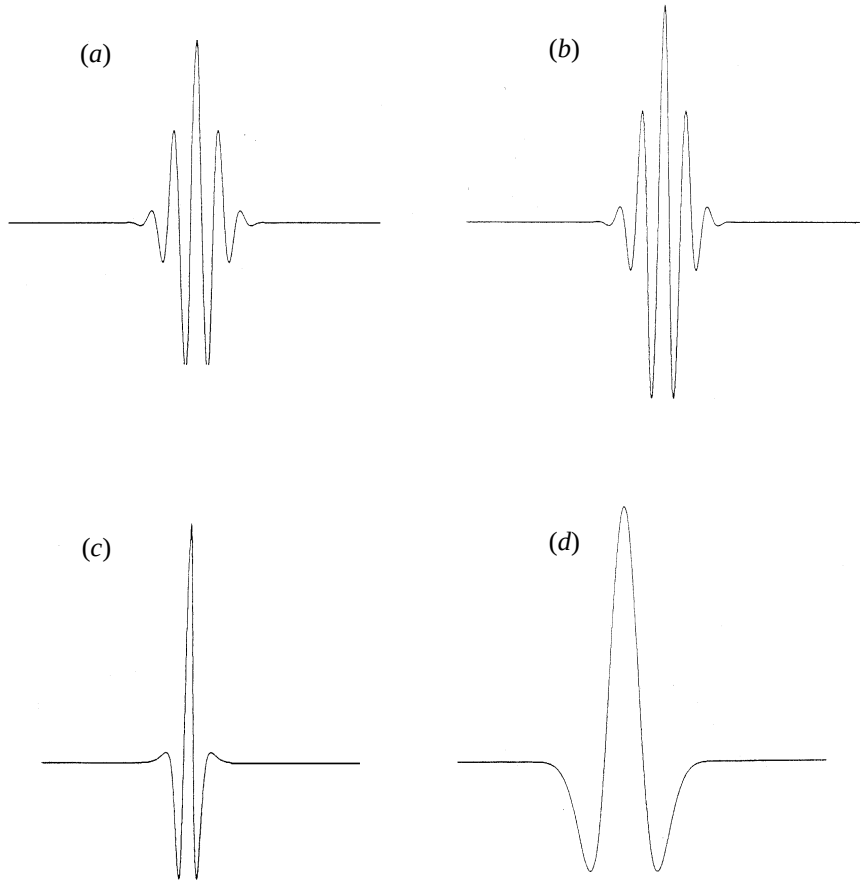

FIGURE 11. Typical analysing wavelets: (*a*) Morlet wavelet; (*b*) modified Morlet wavelet; (*c*) Paul wavelet; (*d*) Marr or 'Mexican hat' wavelet.

Figure 11(*d*) shows the Marr or 'Mexican Hat' wavelet that is obtained using $m = 2$. A progressive wavelet can be constructed from these wavelets by forcing,

$$\hat{\sigma}_m(\omega) = 0 \quad \forall \omega \leqslant 0.$$

Figure 4 shows a section of a velocity record obtained at the edge of the boundary layer during the breakdown of an event. The figure shows a burst of high-frequency oscillations in the form of a wavepacket superimposed on a background T–S signal. Velocity traces from this region of the boundary layer are not contaminated by the events that develop in the central region of the flow and so are amenable to analysis by the WT and global Fourier techniques and hence provide a good test case. The power spectrum of this signal indicated that the frequency of the background T–S waves was approximately 200 Hz and the wavepacket was composed from a narrow band of frequencies centred around 1.2 kHz.

Figure 12(*a–d*) shows contour plots of the modulus of the wavelet coefficients generated by the wavelet analysis of the velocity record using the four progressive wavelets shown in figure 11(*a–d*). The axes of the plots are time and $-\log s$ respectively and are identical. Only the general form of the plots is of interest, thus for clarity the contour levels, which are on identical logarithmic scales, are not labelled.

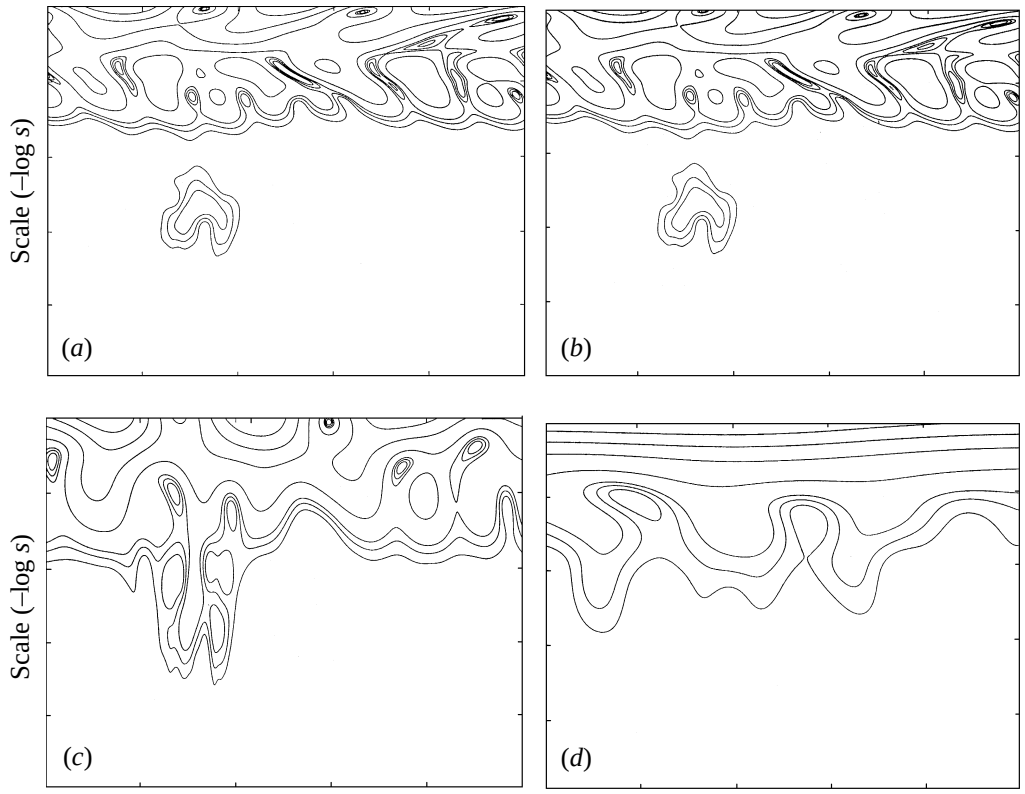

FIGURE 12. Wavelet planes generated from the analysis of the signal given in figure 4 using: (*a*) Morlet wavelet; (*b*) modified Morlet wavelet: (*c*) Paul wavelet; (*d*) Marr or 'Mexican hat' wavelet. Contours on identical logarithmic scales.

Figures 12(*a*) and 12(*b*) obtained by using the Morlet and modified Morlet wavelets respectively, show that these wavelets were able to resolve the scales associated with both the background T–S signal and the high-frequency wavepacket, whereas figures 12(*c*) and 12(*d*) indicate that the Mexican hat and Paul wavelets identified the general T–S signal but smeared the information contained within the burst over a large range of scales. The difference in resolution is due to the frequency-domain characteristics of the respective wavelet filters; a discussion of the characteristics of wavelet filters is given by Farge (1992). On a simplistic level, the Mexican hat and Paul wavelets are better suited to detecting singularities and discontinuities in signals, whilst the Morlet wavelets are more efficient at resolving scale distributions. The modified Morlet wavelet was used in this investigation as this latter property permitted the breakdown of an event to be characterized.

3. Singular spectrum analysis

3.1. *Background*

In general the state of a system at an instant in time can be defined as a position vector, $\boldsymbol{y} = (y_1, y_2, y_3, \ldots)$, in a suitably defined phase space, $\boldsymbol{S}$, whose dimension is given by the number of degrees of freedom of the system. The temporal evolution of the system from an initial state is then given by a trajectory $\boldsymbol{y}(t)$ in this phase space, representing

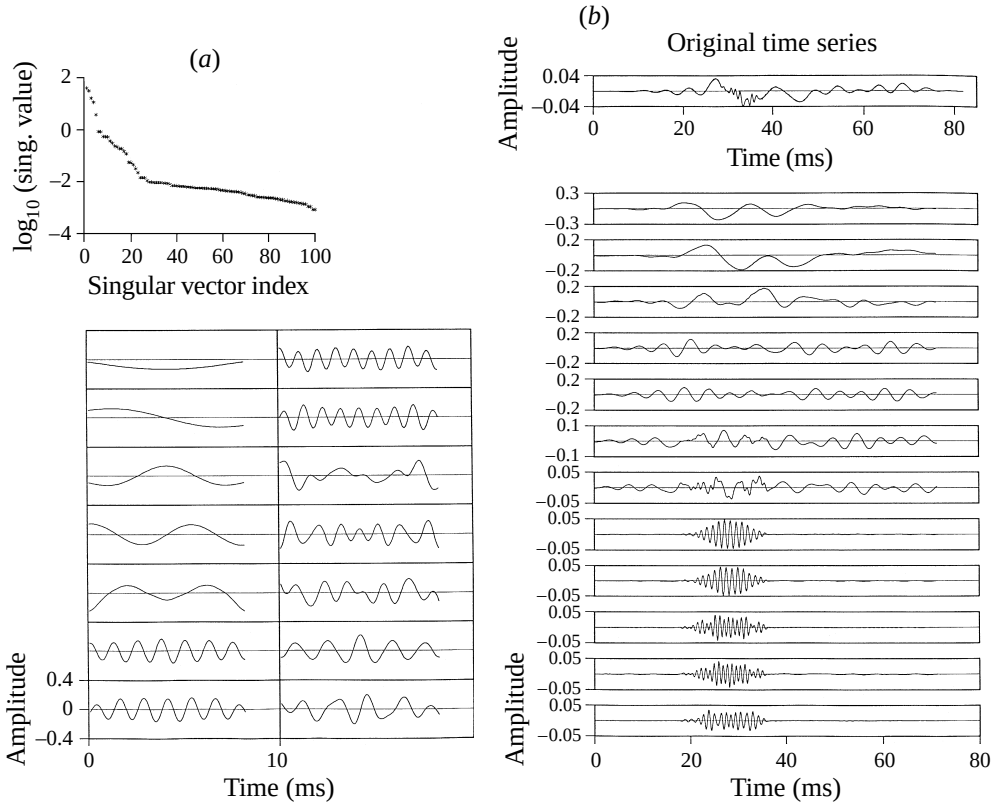

FIGURE 13(*a*, *b*). For caption see facing page.

the solution of the governing equations of motion for the particular initial value. A family of trajectories exists therefore for other initial values and can be considered as a flow in the phase space $\boldsymbol{S}$. Since the majority of dynamical systems of interest are dissipative and exhibit some degree of self-organization, the flow generally contracts onto a lower-dimension sub-manifold, $\boldsymbol{M}$, or phase portrait of the phase space $\boldsymbol{S}$.

Poincaré (1908) (see Bergé, Pomeau & Vidal, 1984) first suggested that a qualitative or geometrical analysis of this phase portrait would provide an insight into the underlying dynamics of the system. However, in general it is not possible to measure the time evolution of all the parameters that define the phase space of a system, or even to decide the relevant properties to measure. However, Takens (1981) linked the phase portrait flowing on $\boldsymbol{M}$ to an embedding of a set of single parameter measurements onto a sub-manifold, $\boldsymbol{U}$, though a diffeomorphism, Φ. The transformation maps trajectories on $\boldsymbol{M}$ to trajectories on $\boldsymbol{U}$ and can be considered as a reversible change of coordinates that distorts the original flow smoothly and preserves topological information. Hence the topological characteristics of the original phase portrait can be studied by examining the reconstructed phase portrait generated from an embedding of the experimental data.

Packard *et al*. (1980) suggested an embedding based on the time derivatives of the data. This method was impractical for noisy finite-precision experimental data and gave no indication of the dimension of the embedding space or how far to proceed in the differential sequence. An alternative approach by Takens (1981) suggested an embedding spanned by vectors that were time-delayed versions of the original time

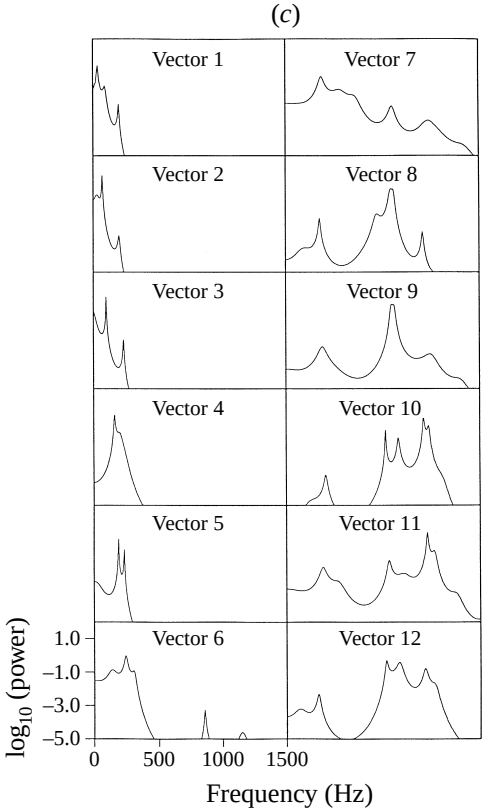

FIGURE 13. (*a*) Singular spectrum for the first 14 singular vectors arranged according to the magnitude of the singular value. The vectors are arranged in descending order of importance and from left to right. (*b*) The original time series and the projection onto 12 energetic singular vectors. The uppermost projection is associated with vector 1. (*c*) The power spectra of the singular vectors given in (*a*). Window length $n = 135$.

series. This technique is known as 'the method of delays' and essentially translates a window through a time series $\boldsymbol{x} = \{v_1, v_2, v_3, \ldots, v_p\}$ that displays n elements with a time delay of τ sample times between the elements. The elements constitute the components of a vector $\boldsymbol{x}_i$ in the embedding space, and the sequence of vectors $\{\boldsymbol{x}_1, \boldsymbol{x}_2, \boldsymbol{x}_3, \ldots, \boldsymbol{x}_p\}$ that are produced as the window is passed over the time series define a trajectory in the reconstructed space.

There are a number of difficulties in applying this method to data obtained from experiment, the most obvious being the choice of the unspecified time scales, τ and n. Broomhead & King (1986) introduced a singular system approach to the method of delays in order to find an optimum basis for the embedding in a least-squares sense. The formulation lead naturally to a description of the system in terms of a Kahunen–Loeve expansion. Vautard, Yiou & Ghil (1992) used this approach to develop a set of algorithms for noise reduction, signal detrending and the identification of signal periodicity. The current work used SSA in a similar vein; here the technique was adapted to detect and track nascent and fully turbulent spots in an automatic manner.

The following subsections give a brief review of the singular system approach of Broomhead & King (1986) and describe the adaptation of the method to spot detection

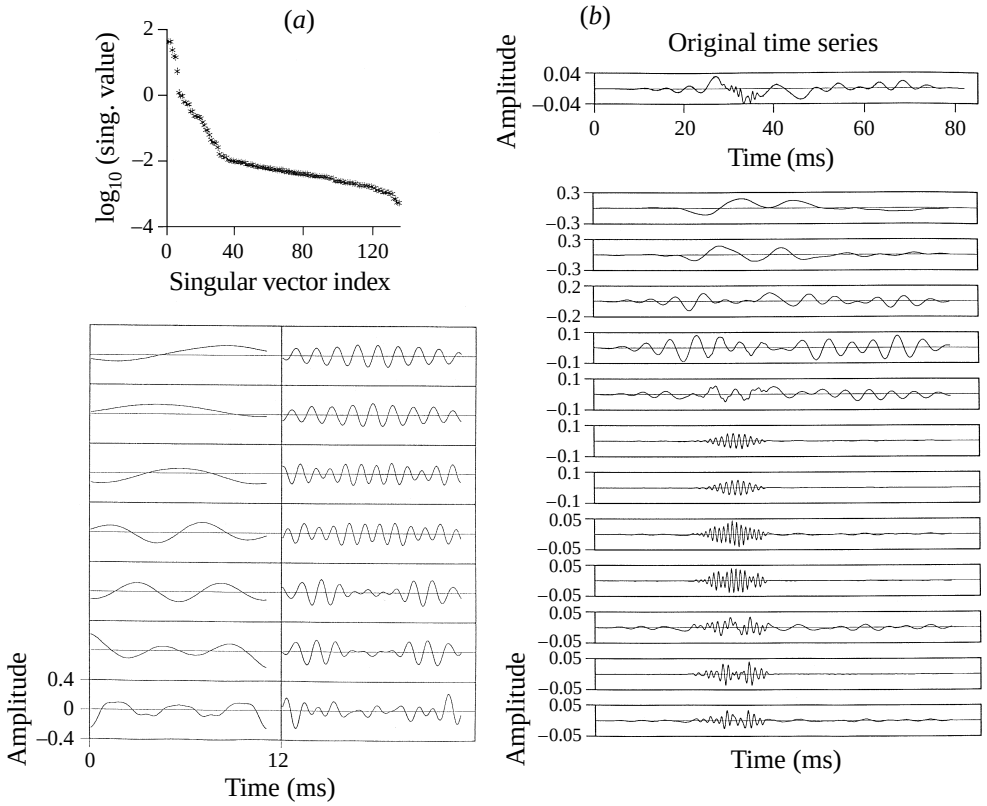

FIGURE 14(*a*, *b*). For caption see facing page.

and tracking as well as the measurement of intermittency. Finally the respective merits of the WT and SSA in the analysis of data from transitional boundary layers are discussed.

3.2. *Implementation and properties*

The approach dispenses with the time lag and passes a window that shows n consecutive elements of a time series that is composed of p elements. This process defines a sequence of $m = p-(n-1)$ position vectors, $\boldsymbol{x}_i$ $(i = 1, \ldots, m)$, that define a trajectory in the reconstructed phase space. The vectors are written in the form of a trajectory matrix, $\boldsymbol{X}$, where

$$\boldsymbol{X} = \begin{bmatrix} \boldsymbol{x}_1^T \\ \boldsymbol{x}_2^T \\ \vdots \\ \boldsymbol{x}_m^T \end{bmatrix}.$$

The following eigenvalue relation can then be written:

$$\boldsymbol{X}^{\mathrm{T}}\boldsymbol{X}\boldsymbol{c}_i = \sigma_i^2 \boldsymbol{c}_i,$$

where $\boldsymbol{X}^T\boldsymbol{X}$ is a real symmetric square matrix that corresponds to the covariance matrix of the components of $\boldsymbol{x}_i$ $(i = 1, \ldots, m)$ that are averaged over the trajectory, i.e. the time-averaged correlation between all pairs of elements in the flow. The vectors $\boldsymbol{c}_i$ $(i = 1, \ldots, n)$ form an optimal set of orthornormal basis functions that span the embedding space. The set of eigenvalues σ_i^2 $(i = 1, \ldots, n)$, known as the 'singular spectrum', corresponds to the mean-square projection of the phase portrait onto the

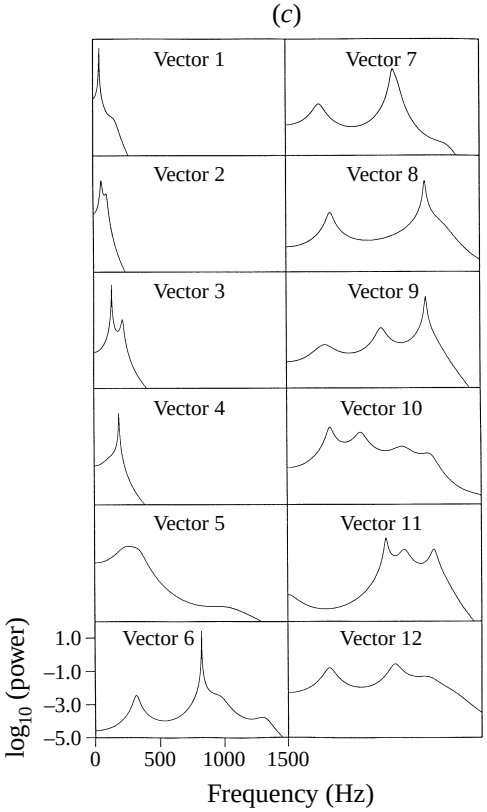

FIGURE 14. As figure 13 but for window length $n = 100$.

basis functions and indicates the degree to which the data explore that direction of the embedding space.

The above eigenvalue relation can be written in the following matrix form:

$$\boldsymbol{X}^T\boldsymbol{X}\boldsymbol{C} = \boldsymbol{C}\boldsymbol{E}^2,$$

where $\boldsymbol{C}$ is the matrix of singular vectors that form the basis of the embedding space and $\boldsymbol{E}$ is a diagonal matrix of the associated singular values. The covariance matrix is rank deficient, thus the solution of the eigenvalue relation is generally obtained using singular value decomposition (SVD). In addition this property implies that a number of the eigenvalues of the system will be zero, or have near-zero values that are associated with the noise floor of the experimental/computational system. The directions with eigenvalues above the noise floor span the embedding space and provide an estimate for the upper bound of the dimension of the phase portrait. An optimized flow in the reconstructed space is therefore generated by the projection of the time series onto those eigenvectors that appear above the noise floor.

The identification of noise-dominated eigenvectors and the resultant partition of the singular spectrum was discussed by Vautard *et al.* (1992). This work also described the identification of signal characteristics such as periodicities and epochs by selective reconstruction in the embedding space. However, the form of the singular spectrum generated from a data set is dependent upon the embedding dimension n. The choice of window length was discussed by Broomhead & King (1986) and more recently by Vautard *et al.* (1992): too small a window may not capture the full dynamics of the system, whereas using a large value of n will generate spurious vectors. Thus the choice

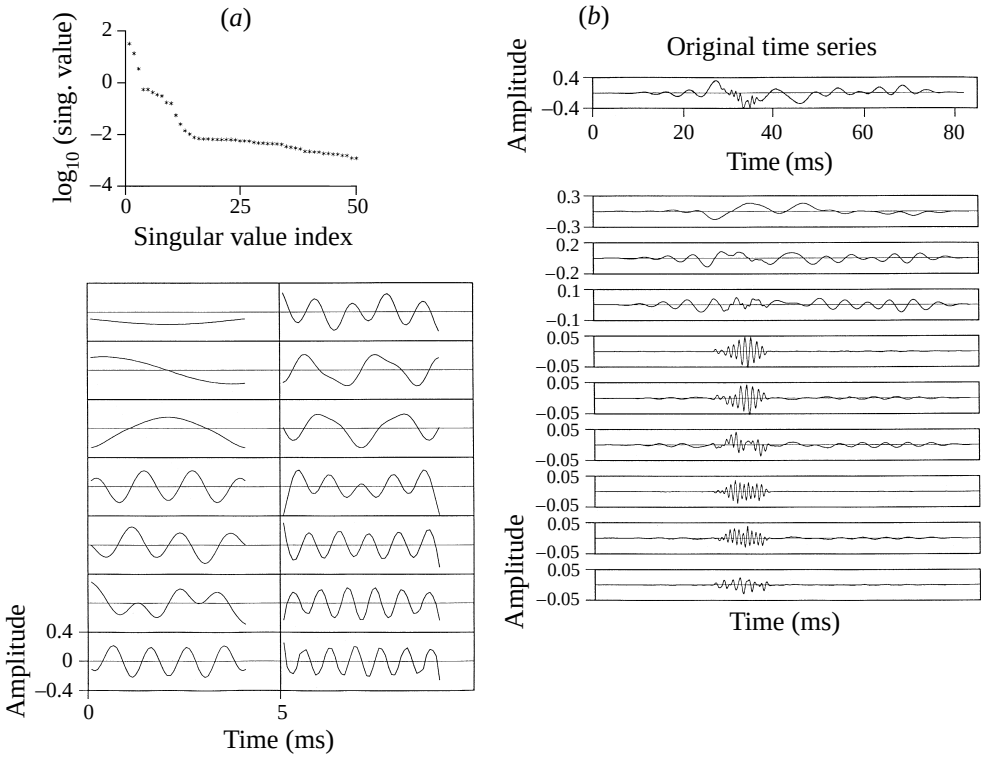

FIGURE 15(*a*, *b*). For caption see facing page.

of window timescale τ_w ($\tau_w = n\tau_s$, where τ_s is the sampling time scale) used in a particular application is dependent on the scale of the signal characteristics of interest. Vautard *et al*. (1992) suggested that for a fixed value of τ_w, SSA is typically successful in analysing periods in the range $(\frac{1}{5}\tau_w, \tau_w)$.

The test data shown in figure 4 were analysed using SSA with window lengths of 135, 100 and 50 sample steps that corresponded to time scales of 0.0108 s, 0.008 s, 0.004 s (or 2.16 τ_{TS}, 1.6 τ_{TS}, 0.8 τ_{TS}, where τ_{TS} is a typical T–S time scale) respectively. Figure 13(*a*) shows the singular spectrum generated from the data set with $n = 135$, and the form of the first 14 singular vectors whose singular values account for more than 95% of the signal energy. The spectrum can be divided into three distinct regions. The majority of the signal energy can be associated with the first region that contains the first six singular values, thus the major signal dynamics are contained on a low-dimension sub-manifold of the phase space. The eigenvectors are approximately sinusoidal and the spectrum indicates that some of the vectors are 'paired'. Vautard *et al*. (1992) linked pairing to the existence of significant periodicity in a signal, thus SSA identified two dominant time scales, 0.4 τ_{TS} and τ_{TS}, in the test data that correspond to T–S and subharmonic disturbances in the flow.

The second region identified in the singular spectrum is less distinct and contains approximately 30 singular values. Once again the associated singular vectors are sinusoidal, but become increasingly irregular as the singular value decreases. Pairing is also evident in the spectrum and is associated with time scales 4.2 τ_{TS} and 5.7 τ_{TS} that are linked to the high-frequency burst evident in the velocity record. The remainder of the singular values comprise the third region of the singular spectrum and indicate the noise floor of the computational and experimental system.

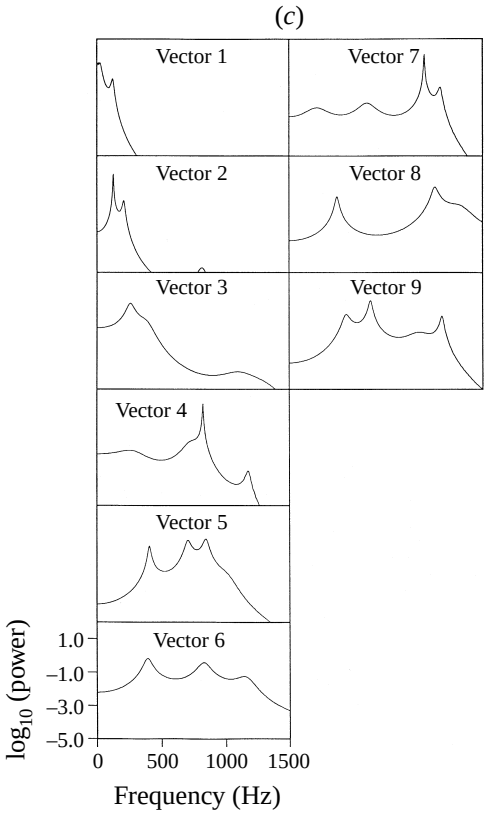

FIGURE 15. As figure 13 but for window length $n = 50$ and only nine energetic singular vectors in (*b*)

Figure 13(*b*) compares the original time series with the projection of the data onto the first twelve eigenvectors. The first two projected vectors appear to be smoothed or filtered versions of the original time series: the higher frequency oscillations have been removed and the general variation of the signal has been preserved. The remaining projections from this region of the spectrum also show filtered signals but with a different pass band. The projections associated with the second region of the spectrum are significantly different and generally show a high-frequency wavepacket of oscillations in the centre of the record. These signals appear to be the result of a sharper pass-band filter that is ringing at the average frequency of the filter. The ringing is centred on the location of the high-frequency burst in the original signal but the time-domain resolution of the burst is poor. These projected vectors correspond to eigenvectors that are attempting to capture the structure of the original burst. Thus these vectors not only characterize the spectral or scale composition of the original signal but also the form of these components in the time domain.

The projection of the data set onto the singular vectors can be viewed as the action of linear filters in the Fourier plane, where the eigenvectors represent the impulse response of the filters. Figure 13(*c*) shows the Fourier-domain representation of these filters calculated using the maximum entropy method (MEM). The diagram clearly shows the differing pass-band characteristics of the filters in the Fourier domain.

Figure 14(*a–c*) shows the corresponding diagrams for a window length of $n = 100$. The singular spectrum and vectors in figure 14(*a*) show similar characteristics to those

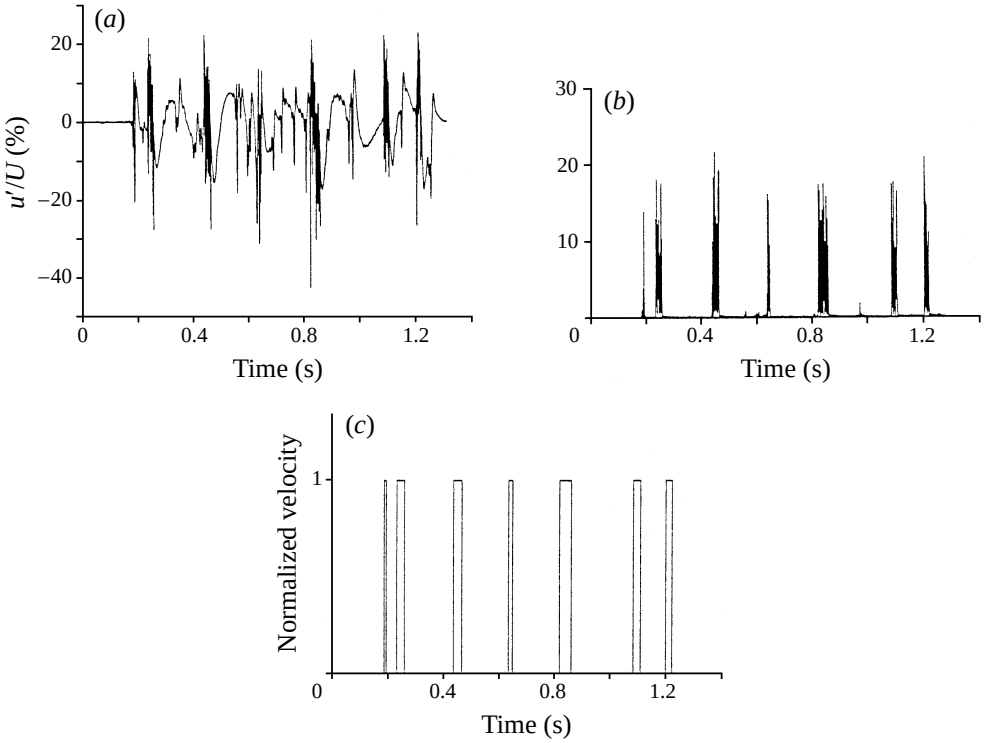

FIGURE 16. Demonstration of the spot detection procedure using SSA: (*a*) original hot-wire time series showing turbulent spots; (*b*) resultant signal after projection and Hilbert transform; (*c*) normalized signal showing locations of turbulent spots.

observed with embedding dimension 135. The major difference between the two embeddings is the reduced number of singular vectors that appear above the noise floor. This reduction can be viewed as a coarsening of the spectral resolution of the decomposition as shown in figure 14(*c*); however, figure 14(*b*) shows that the temporal resolution of the filtered burst has improved. These trends continue with an embedding dimension of 50 as shown in figure 15(*a–c*). A reduction in window length therefore results in improved temporal, but reduced spectral, resolution of the high-frequency burst.

3.3. *Spot detection and tracking*

With an appropriate choice of embedding dimension and characteristic singular vector, SSA can be used as a detection procedure for the occurrence of intermittent high-frequency oscillations in the velocity records. These regions of the time series are usually associated with nascent or fully turbulent spots, thus SSA can be used as an automatic spot detection technique.

A range of velocity records from a number of regions of a transitional boundary layer were analysed using SSA with a range of embedding dimensions. An optimum embedding that generated the minimum number of high-frequency singular vectors was then chosen. The subsequent projection of the original data onto these vectors accurately resolved the location of the high-frequency spot structures in the time series. Figure 16 demonstrates the application of this procedure. A typical hot-wire record from the latter highly intermittent region of transition is given in figure 16(*a*). The trace contains localized regions of high-frequency oscillations, indicating the passage of a turbulent spot over the hot-wire probe, superimposed on an unsteady background

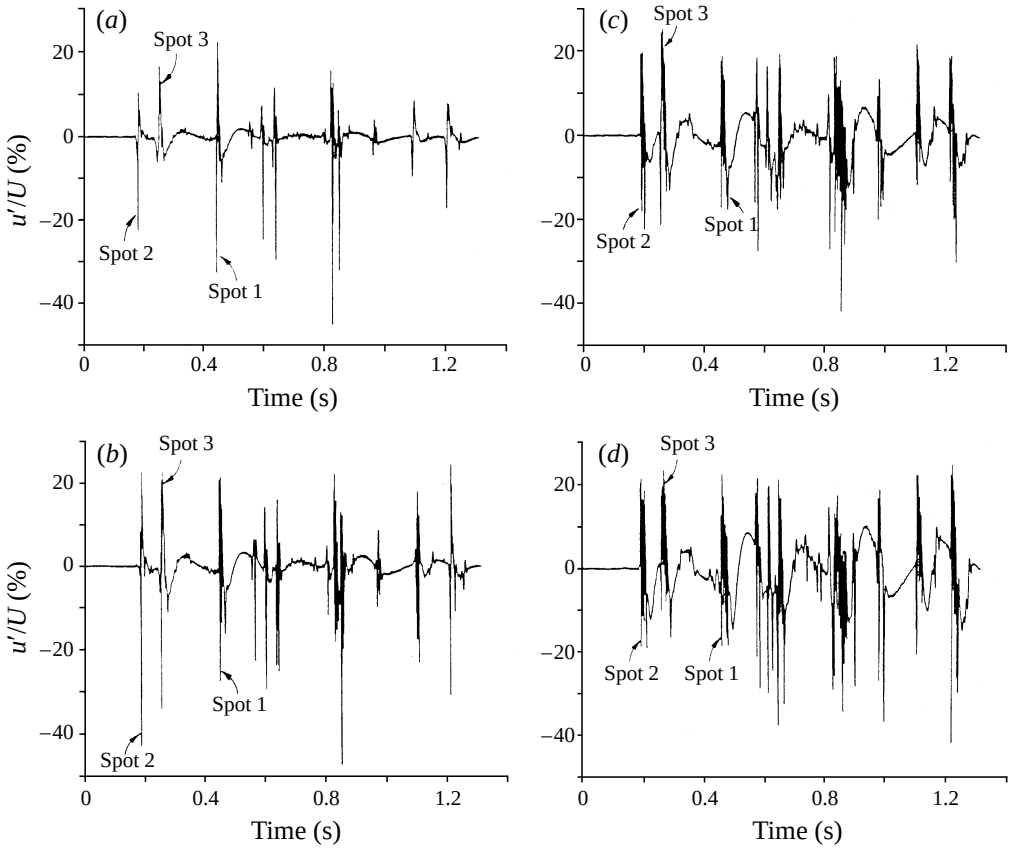

FIGURE 17. Fluctuating streamwise velocity signal showing incipient turbulent spots at $z = 0.02$ m: (*a*) $x = 1.1$ m; (*b*) $x = 1.15$ m; (*c*) $x = 1.2$ m; (*d*) $x = 1.25$ m.

signal. Figure 16(*b*) shows the Hilbert transform of the result of the projection of the original time series onto the chosen singular vector. The figure indicates that this primary processing has removed the unsteady background signal, leaving localized bursts of oscillations that mark the leading and trailing edges of the spots. The amplitude of the burst is directly proportional to the amplitude of the high-frequency oscillations in the original time series, thus an unambiguous threshold criterion based on signal amplitude was then used to generate the normalized plot shown in figure 16(*c*).

Therefore, it can be seen that SSA can be used to extract the location and time duration of high-frequency bursts of oscillations within a hot-wire record. This information was used by Shaikh & Gaster (1994*b*) to calculate the intermittency of transitional boundary layer flows and to extract bursts automatically from the original signal for further processing by the WT. The extraction process was tested extensively and was found to be accurate even for low levels of the intermittency parameter. In addition, the information provided on the location of spot interfaces was used in conjunction with white-noise excitation to track individual turbulent spots and hence investigate the distribution of spot inception locations and the propagation characteristics of mature turbulent spots.

Figure 17(*a–d*) shows velocity records obtained from four consecutive streamwise locations at a single spanwise position in the final turbulent spot region of transition.

The signals correspond to 'single-shot' recordings of the response of the boundary layer to a single white-noise sequence and are not averaged in any way. Figure 17(*a*), corresponding to the most upstream location, shows a signal containing violent events or excursions separated by regions of relative inactivity. Although the events differ from one another in their detail and peak amplitude there is some similarity in the overall pattern.

Figure 17(*b*) shows the measured response at a location 50 mm further downstream. The events in this signal occur at the same relative positions as those shown in figure 17(*a*) and it is clear that the generation of these excursions is deterministic and controlled by the input excitation. The figure indicates that spot 1 has developed high-frequency oscillations whilst the remaining major excursions have increased in amplitude compared to the previous measurement station. Figures 17(*c*) and 17(*d*) characterize the subsequent development of the flow field and show that spots 2 and 3 also develop high-frequency oscillations. In particular, previously observed weak excursions or young events have increased in amplitude, whereas more mature events appear to saturate and develop structures containing high-frequency oscillations that are indicative of the formation of turbulent spots in the flow.

Thus even on a single-shot basis, the white-noise technique generates spots in a deterministic manner. Although the internal structure of the high-frequency disturbances may not be repeatable from realization to realization, the location of the structures is determined by the input excitation. Thus hot-wire records associated with individual spots can be correlated in the streamwise and spanwise directions by assuming that high-frequency oscillations with intersecting interface locations are associated with the same spot. This technique therefore permits individual turbulent spots to be followed as they propagate downstream.

3.4. *Comparison of SSA and the WT*

SSA and the WT are both techniques that can be used to examine the local as well as the global signal characteristics. The WT projects the signal onto a set of basis functions that are localized simultaneously in the temporal and spectral domains. The basis functions are generated from scaled versions of a single mother function, thus a one-dimensional signal is mapped on to a two-dimensional time-scale plane in which localized signal information is retained locally in the transform plane. The method essentially substitutes the frequency decomposition of the global Fourier transform for a decomposition based on the size or scale of an analysing function. The transform or wavelet plane contains information from both the analysing wavelet and the signal, thus the choice analysing wavelet in a particular application is dependent on the signal characteristics of interest.

SSA, on the other hand, generates an optimum signal-adaptive set of basis vectors at the scale of the embedding dimension. These vectors have been used as a set of analysing functions to generate a decomposition at one particular scale in a similar vein to the STFT. The STFT, however, uses trigonometric basis vectors: the advantage of SSA is that the set of analysing functions is chosen naturally from the data set. Although SSA is essentially a linear analysis method, the data-adaptive nature of the technique leads to the generation of basis vectors better suited to describing nonlinear systems than spectral decomposition methods.

Both techniques require some input concerning the signal characteristics of interest, i.e. the choice of analysing function in the WT and the embedding dimension used in SSA. The techniques are therefore extremely versatile and have been used in a number of different applications, see Farge (1992) and Vautard *et al.* (1992). In the current

work, the WT in conjunction with the modified Morlet wavelet was used to investigate and describe fine structure of the localized breakdown of the flow to high-frequency disturbances and the formation of turbulent spots. In contrast, SSA was used to describe global behaviour of the resultant intermittent flow field and in particular the growth characteristics of spots.

4. Experimental details

4.1. *Apparatus and procedure*

The experiments were performed on a flat plate mounted vertically in the 3 ft square working section of the closed-return low-turbulence wind tunnel at Cambridge University†. The turbulence intensity of this facility is less than 0.01% at a tunnel speed of 18 m s^{-1} within the frequency band 4 Hz to 4 kHz. This facility was used in the previous experiments of Gaster (1990) and has generated consistently low levels of free-stream turbulence and is therefore ideally suited for investigations of this type.

The plate was 1.68 m in length and incorporated a small loudspeaker buried on the centreline at a distance 205 mm from the leading edge. A zero pressure gradient was maintained over the first 1 m of the plate by the adjustment of a two-component flap mounted at the trailing edge. The origin of the coordinate system used in this investigation was situated on the centreline, at the leading edge of the plate: x corresponds to the streamwise ordinate, y the ordinate perpendicular to the wall and z the spanwise ordinate.

Flow measurements were made with constant-temperature hot-wire anemometry. The position of the boundary layer probe, data acquisition and the excitation of the boundary layer were controlled by a micro-computer. A single time base was used to control both the digital-to-analogue converter feeding the embedded speaker and the signal acquisition analogue-to-digital converter so that the two processes were synchronized.

Boundary layer traverses were made with the hot wire to ensure that the mean flow velocity profiles were of the correct Blasius form. The measured velocities were fitted to the theoretical profile in order to estimate the position of the wall. An automatic iterative scheme was used to locate the probe at a point in the Blasius profile that had a particular velocity ratio with respect to the free stream. It was then a simple matter to re-position the probe to the required non-dimensional distance from the wall, η, given by

$$\eta = y(U/2\nu x)^{1/2}.$$

The free-stream velocity was set at 18 m s^{-1} for these experiments. The boundary layer that developed on the flat plate was excited repeatedly with computer-generated white noise. The amplitude of the excitation signal was chosen so as to ensure there were no gross distortions of the flow field local to the acoustic source and that initial upstream boundary layer disturbances were of a small amplitude.

4.2. *The white noise*

The white noise was designed to excite a wide spectral range of disturbance waves. A sequence was produced by specifying the desired Fourier domain characteristics of the signal and then performing an inverse FFT to generate a time series. The magnitude of each of the signal Fourier coefficients was stipulated whilst the phase was

† Now at the Engineering Department, Queen Mary and Westfield College, London, UK.

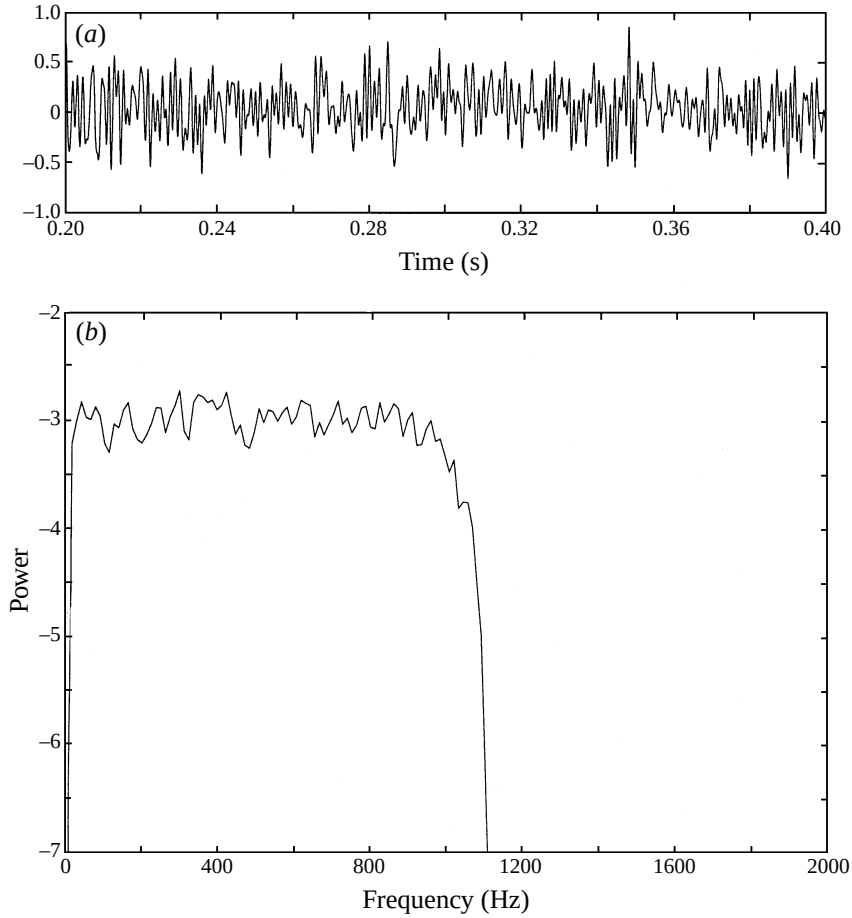

FIGURE 18. (*a*) Section of white-noise excitation signal and (*b*) its power spectrum.

randomized in the range 0 to 2π. Figure 18(*a*) shows a white-noise signal generated in this way and figure 18(*b*) shows the associated power spectrum.

5. Structure of an event

5.1. *Background and experimental parameters*

This experiment aimed to measure the time history of a y, z slice of the disturbance flow field prior to breakdown in the neighbourhood of a large-amplitude event. A one kilobyte record of computer-generated white noise was used to excite the boundary layer via the buried loudspeaker. Previous preliminary experiments had indicated that this section of the white-noise time series generated an event in the flow. The boundary layer response was measured at 14 spanwise stations, $25 \geqslant z \geqslant -40$ mm, and 15 locations normal to the wall, $4.5 \geqslant \eta \geqslant 0.4$, at a single streamwise position 790 mm from the leading edge of the plate, for $Re_{\delta*} \approx 1700$ ($Re_x = 971\,300$). In comparison, the breakdown of the event and the appearance of high-frequency disturbances was observed at $Re_{\delta*} \approx 1720$.

The boundary layer was artificially excited with the same noise record 62 times at each measurement location so that the ensemble-averaged response could be obtained. The fluctuating component of the streamwise velocity was preamplified and passed

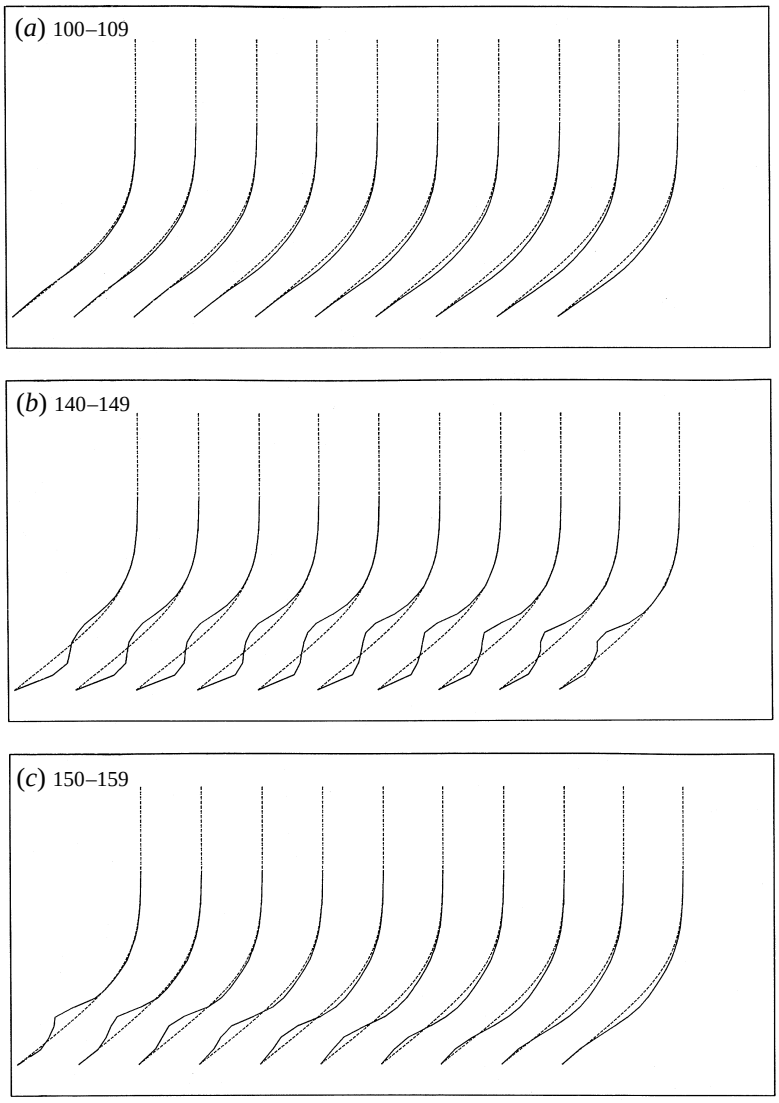

FIGURE 19. Temporal development of averaged centre-line velocity profiles (solid line) compared to the theoretical Blasius profile (dashed line). Time duration 0.002 s. Sample times (*a*) 100–109; (*b*) 140–149; (*c*) 150–179.

through a 4–2000 Hz pass-band filter before being sampled at a rate of 5 kHz. A second channel digitized the total streamwise velocity at the same rate.

Preliminary results from this experiment were presented briefly in Shaikh & Gaster (1994*a*); a more detailed description and analysis of the experimental measurements is given in the following subsection.

5.2. *Results*

5.2.1. *Total velocity*

Figure 19(*a–c*) shows snapshots of the temporal development of the ensemble-averaged velocity profiles obtained on the centreline ($z = 0$); the time duration is 0.002 s (0.4 τ_{TS}). The dashed curves represent the theoretical Blasius profile, whilst the

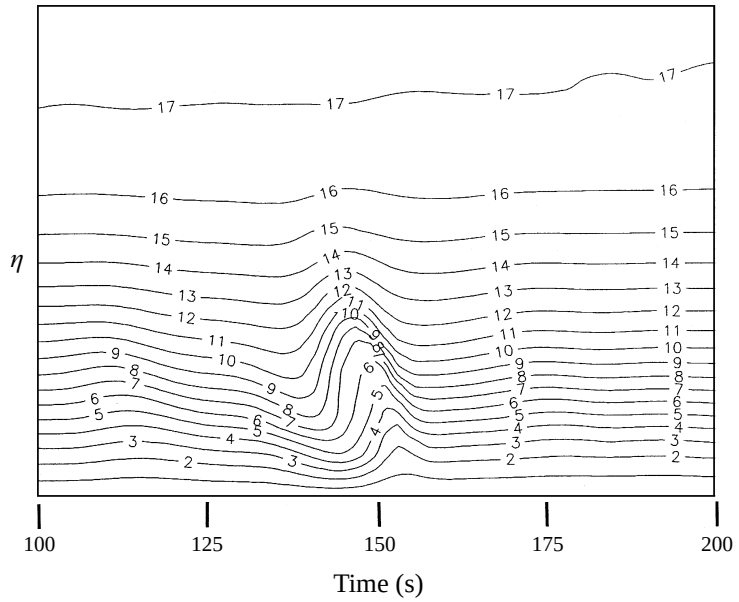

FIGURE 20. Contour plot of averaged centreline velocity measurements for sample times 100–200.

solid lines show the unsmoothed ensemble-averaged experimental data. Complete profiles were generated by a linear extrapolation from the near-wall station ($\eta = 0.3$) to the origin. The numbers indicated on the figures are markers to aid the comparison of the figures and correspond to sample time indicies.

Figure 19(*a*) shows that, except for the first marginally inflectional profiles, the profiles tend to become progressively fuller than Blasius with time. Earlier profiles in this sequence are not shown as they were indistinguishable from Blasius. This trend continues and is then followed by the gradual formation of an inflectional profile and associated regions of high shear that intensify dramatically as shown in figure 19(*b*). The following sequence, figure 19(*c*), shows that the profiles then become progressively less inflectional, the regions of high shear weaken and a fuller velocity profile is formed once again. The profiles subsequently decay to the background Blasius form.

Figure 20 shows a contour plot of the ensemble-averaged centreline velocity profiles calculated from the full data set. The sample time instants indicated on figure 19 are marked for clarity. The figure shows that in this plane the event corresponds to a highly localized coherent flow structure that can be interpreted as a downwards sweep of high-velocity fluid followed by a more energetic upwards sweep of low-velocity fluid. The figure also shows two regions of high shear in the neighbourhood of the event: the most energetic is associated with the upwards sweep in the central region of the boundary layer, whilst the weaker region occurs near the wall.

These figures indicate that the flow field in the neighbourhood of an event is complex and highly three-dimensional and that significant changes in the distribution of vorticity occur over very short time scales. The three-dimensional nature of the flow field can be seen more clearly in the contour plots of the ensemble-averaged velocity in the (z, y)-plane shown in figure 21(*a–c*). The figures correspond to snapshots of the flow field at selected time instants.

Figure 21(*a*), corresponding to $t = 135$, shows significant spanwise structure, and the flow field is approximately symmetric and appears to consist of a single up-sweep

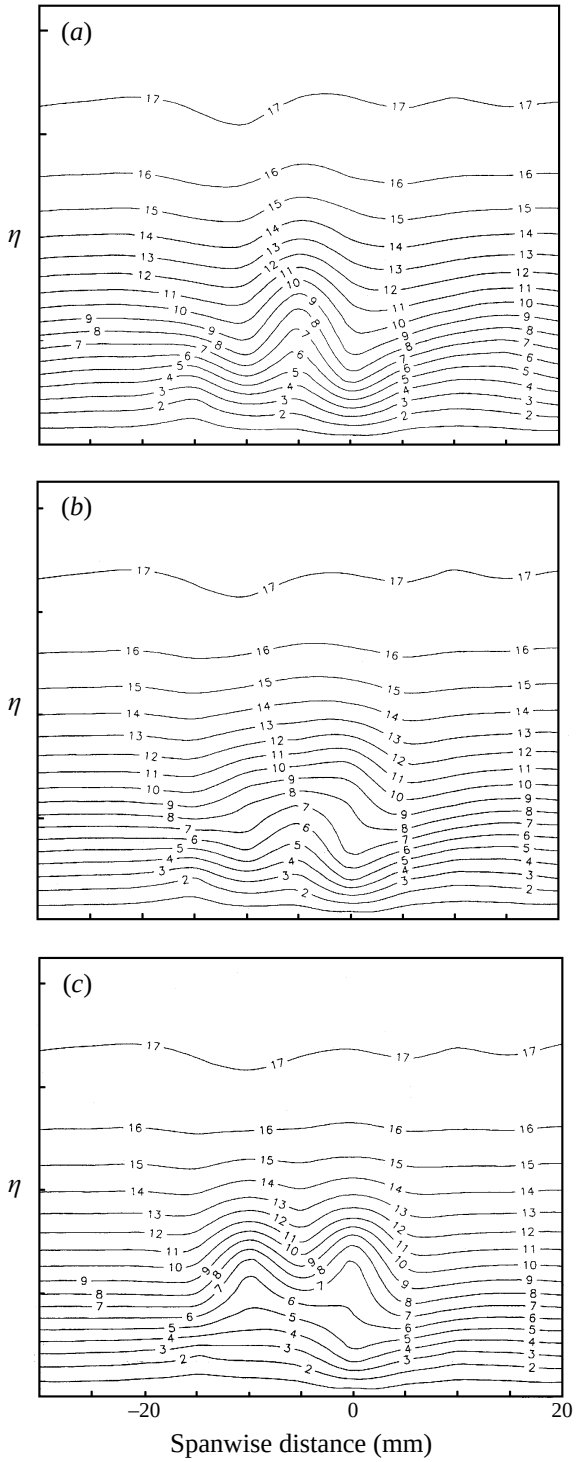

FIGURE 21. Contour plot of the averaged velocity measurements in the (y, z)-plane at three time instants: (*a*) $t = 135$; (*b*) $t = 140$; (*c*) $t = 145$.

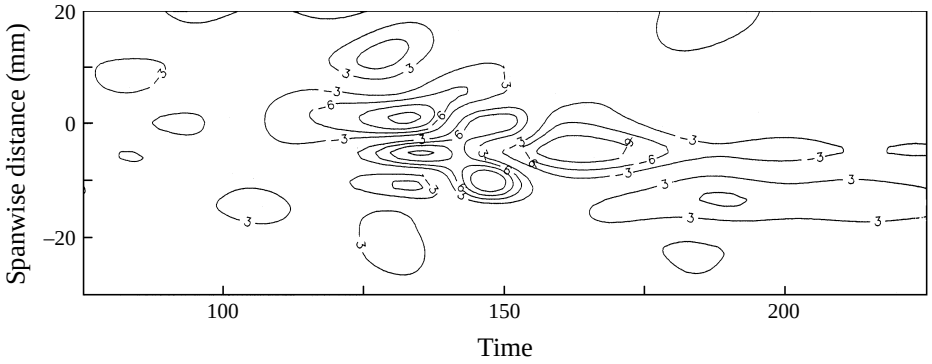

FIGURE 22. Contour plot of the percentage deviation of the experimentally determined displacement thickness from the theoretical Blasius value in the time–span plane.

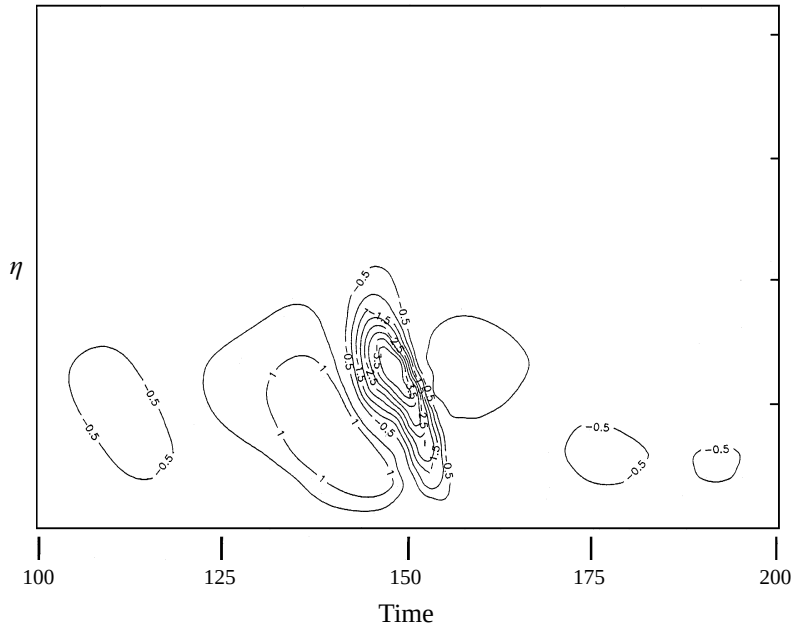

FIGURE 23. Contour plot of averaged fluctuating centreline velocity measurements for sample times 100–200.

and two down-sweeps of fluid. The 'full' centreline profiles identified in figure 19(*c*) are associated with the development of the down-sweep in the flow. This structure initially intensifies with time; however, the subsequent development of the inflectional velocity profiles in figure 19(*c*) is associated with the formation of two low-shear regions or 'eyes' in figure 21(*b*) at $t = 140$. These can be seen more clearly in figure 21(*c*) at $t = 145$, and are linked to the development of two corresponding high-shear regions in the flow. A comparison of the figures shows that the character of the flow field has reversed over the time interval 0.003 s (or 0.4 τ_{TS}): the flow now consists of a single down-sweep and two up-sweeps of fluid. Further measurements show that the structure decays with time and the flow field tends to the Blasius form.

Finally, figure 22 shows a contour plot of the percentage deviation of the experimentally determined displacement thicknesses from the theoretical Blasius value

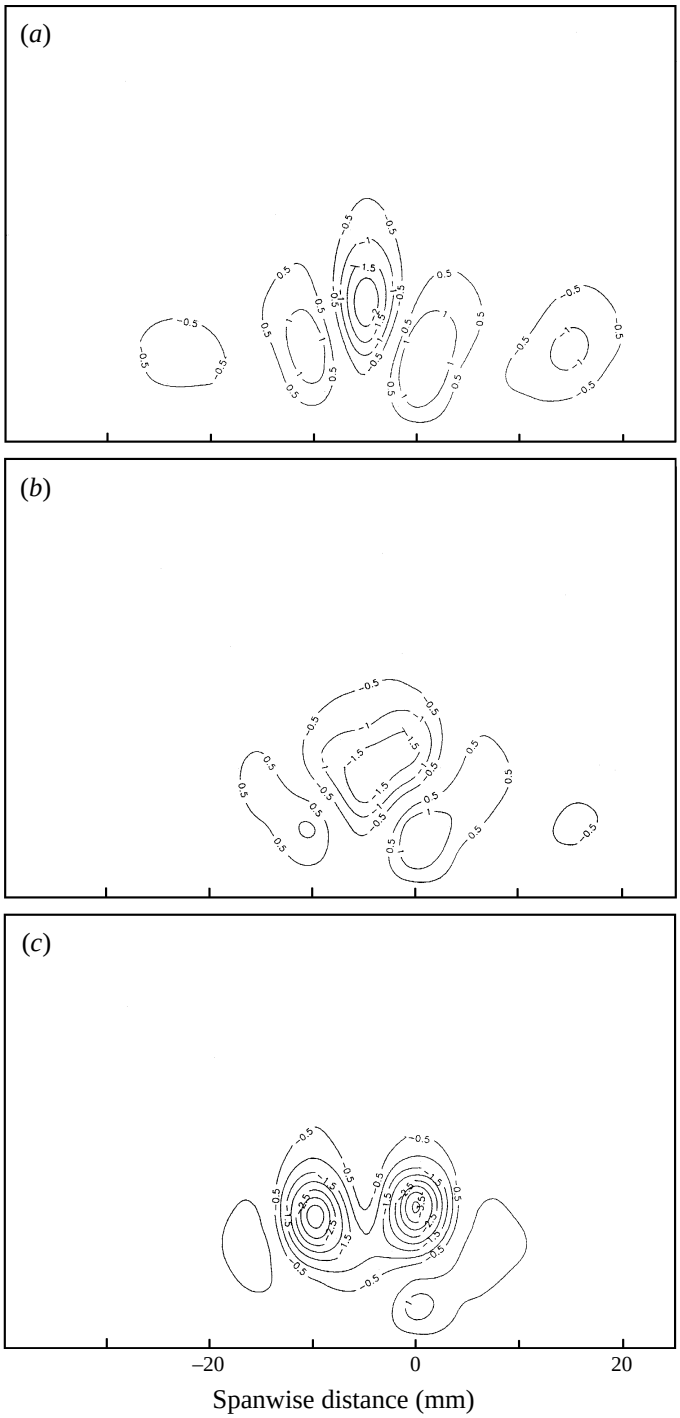

FIGURE 24. Contour plot of the averaged fluctuating velocity measurements in the (y, z)-plane at three time instants: (*a*) $t = 135$; (*b*) $t = 140$; (*c*) $t = 145$.

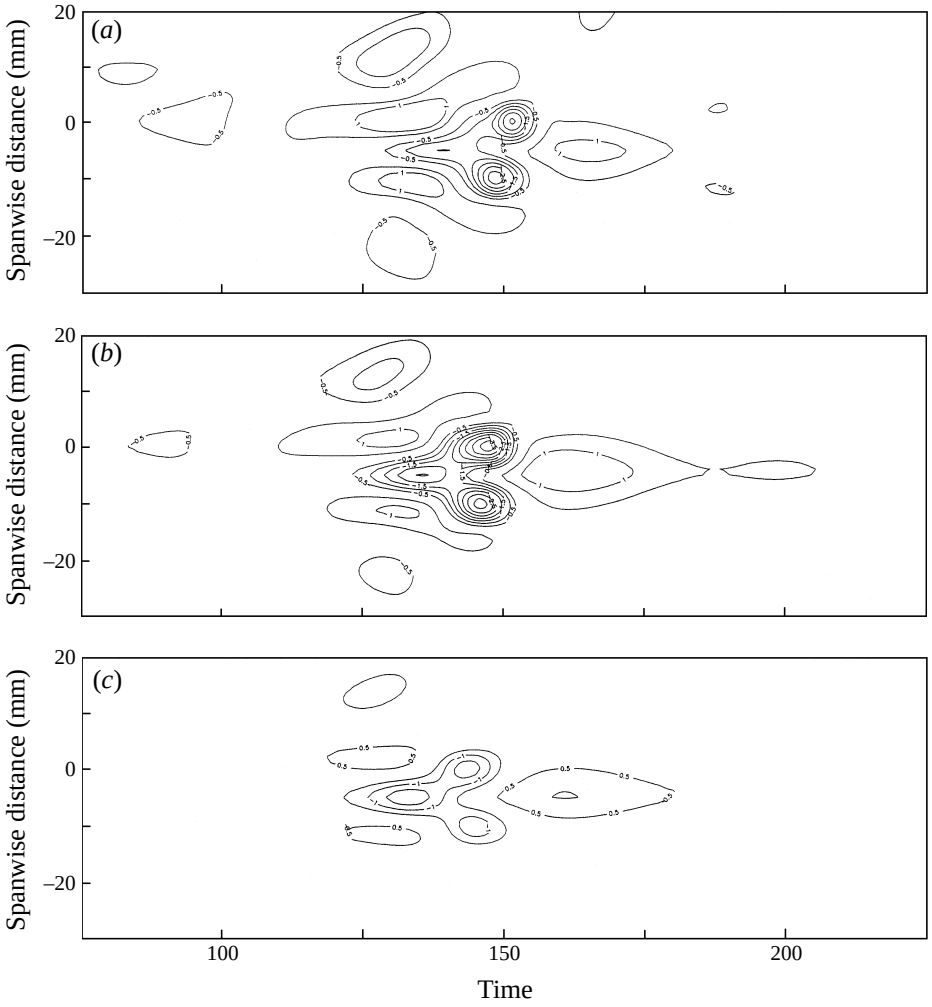

FIGURE 25. Contour plot of the averaged fluctuating velocity measurements in the time–span plane at (*a*) $\eta = 0.9$, (*b*) $\eta = 1.1$, (*c*) $\eta = 1.7$.

in the span–time plane. Once again the time axis is indexed for clarity. The plot shows that this displacement surface is highly three-dimensional with a maximum deviation of $\pm 12\%$ from the Blasius value.

5.2.2. *Fluctuating velocity*

Figure 23 shows a contour plot of the temporal development of the ensemble-averaged fluctuating streamwise velocity on the centreline ($z = 0$) and is the unsteady counterpart of figure 20. The figure consists of five coherent region of alternating sign; the gross up-sweep and down-sweep identified in figure 20 can be associated with the two energetic central regions. Although the hot wire measured the fluctuating streamwise velocity only, it is clear that the coherent regions in figure 23 correspond to coherent structures propagating in the flow.

The highly three-dimensional character of an event is shown in figure 24(*a–c*), which is the fluctuating counterpart to figure 21(*a–c*). Figure 24(*a*), at $t = 135$, shows that once again the unsteady velocity field is characterized by coherent regions of alternating

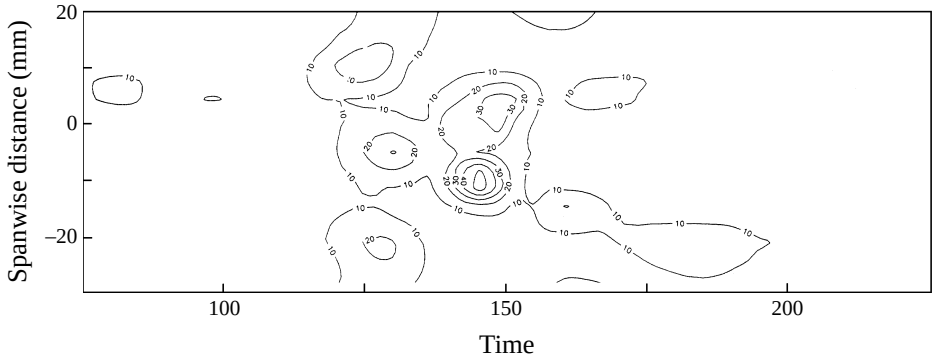

FIGURE 26. Contour plot of the repeatability, $\sigma U\,\%$, of the fluctuating velocity measurements in the time–span plane at $\eta = 1.1$ (figure 25*b*).

sign centred on the locations of the gross up- and down-sweeps. The spanwise extent of the event is approximately 50 mm or $36\delta^*$ at this streamwise location. The following figures show that the central negative region broadens at $t = 140$ during the development of the eyes in figure 21(*c*) and divides into two 'legs' at $t = 145$ that are associated with the high-shear regions. The temporal decay of the structure is characterized by the legs dividing, decreasing in energy and moving closer to the wall. Later measurements indicate that the event develops a central positive region corresponding to the development of a full velocity profile.

The streamwise structure of the disturbance field is seen more clearly in figure 25(*a–c*) that shows span–time plane views of the fluctuating velocity field at a number of non-dimensional heights from the wall. Figure 25(*a*) at $\eta = 0.9$ indicates that the majority of the signal energy is contained within five spanwise coherent regions of alternating sign near $t = 125$. There is also evidence of significant signal energy upstream and downstream of this location at $t = 100$ and $t = 175$ respectively. This picture of the highly three-dimensional structure of the fluctuating flow field is consistent with previous views of the flow field.

The initial development of the flow field with distance from the wall is shown in figure 25(*b*) corresponding to $\eta = 1.1$. The figure shows that the central negative region has intensified and evolves into a Λ-shaped form; the remainder of the disturbance field shows little change over this non-dimensional distance except for the formation of a large positive or 'calmed' region near $t = 150$. Moving further from the wall, figure 25(*c*) corresponding to $\eta = 1.7$ shows that the energetic structures decay, indicating that the majority of the signal energy is concentrated in the lower region of the boundary layer centred near $\eta = 1.1$.

Although the temporal position of the event in the time series is repeatable between realizations of the excitation, §1.2 indicated that the amplitude of an event showed considerable variation from one record to another immediately prior to breakdown. Figure 26 shows a contour plot of a measure of the repeatability of the disturbance field given in figure 25(*b*). The plot shows contours of $\sigma/U\,\%$, where σ represents the 90 % confidence level for the standard deviation of the velocity records and U is the free-stream velocity. The figure shows that significant sample-to-sample variation is concentrated in coherent regions coincident with the energetic structures identified in figure 25(*b*). In particular, the largest values of $\sigma/U\,\%$ are associated with the negative Λ-shaped structure, indicating that the sample-to-sample variation arises from differences in amplitude rather than in spatial position. This is also true for the

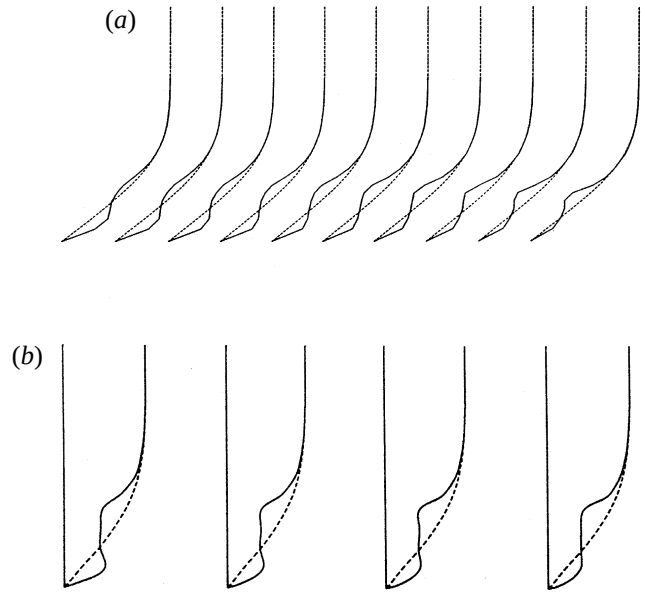

FIGURE 27. Typical velocity profiles obtained from: (*a*) the current white-noise experiment; (*b*) the wavepacket experiment of Gaster (1993).

secondary positive structures; however, the $\sigma/U\,\%$ contours associated with the outlying negative structures are more diffuse, indicating that their temporal positions may vary.

5.3. *Discussion*

The naturally excited experiments discussed in §1.2 identified the appearance of an 'event' in the hot-wire records at the essential precursor to the formation of a turbulent spot in a boundary layer flow. This experiment used the white-noise technique to examine the three-dimensional structure of an ensemble-averaged event immediately upstream of the breakdown of the flow to high-frequency disturbances. The hot-wire measurements indicated that the event was linked to a highly three-dimensional complex vortical structure or entity propagating in the streamwise direction.

Ensemble-averaged velocity profiles obtained from the midplane of the event structure showed that significant changes in the distribution of vorticity occurred over very short temporal and hence spatial scales. In particular, the central region of the structure was characterized by the rapid development of highly inflectional velocity profiles and associated regions of high shear, followed by a 'calmed' zone of fuller profiles. Sequences of profiles from other planes within the disturbance field also indicated that rapid redistribution of spanwise and streamwise vorticity occurred within the body of the event structure, generating a three-dimensional 'displacement surface'. This may provide a clue to the physical mechanisms responsible for the formation and development of the event structure. Doorly & Smith (1992) and Smith, Dodia & Bowles (1994) describe the transitional flow field in terms of a three-dimensional unsteady Euler flow that exhibits a three-dimensional triple-deck structure with a pressure–displacement interaction. The development of the displacement surface suggests that such an interaction may be driving the nonlinear evolution of this flow field.

The vortical nature of the flow field was more evident in the fluctuating velocity measurements. These showed an inclined central Λ-shaped negative region with

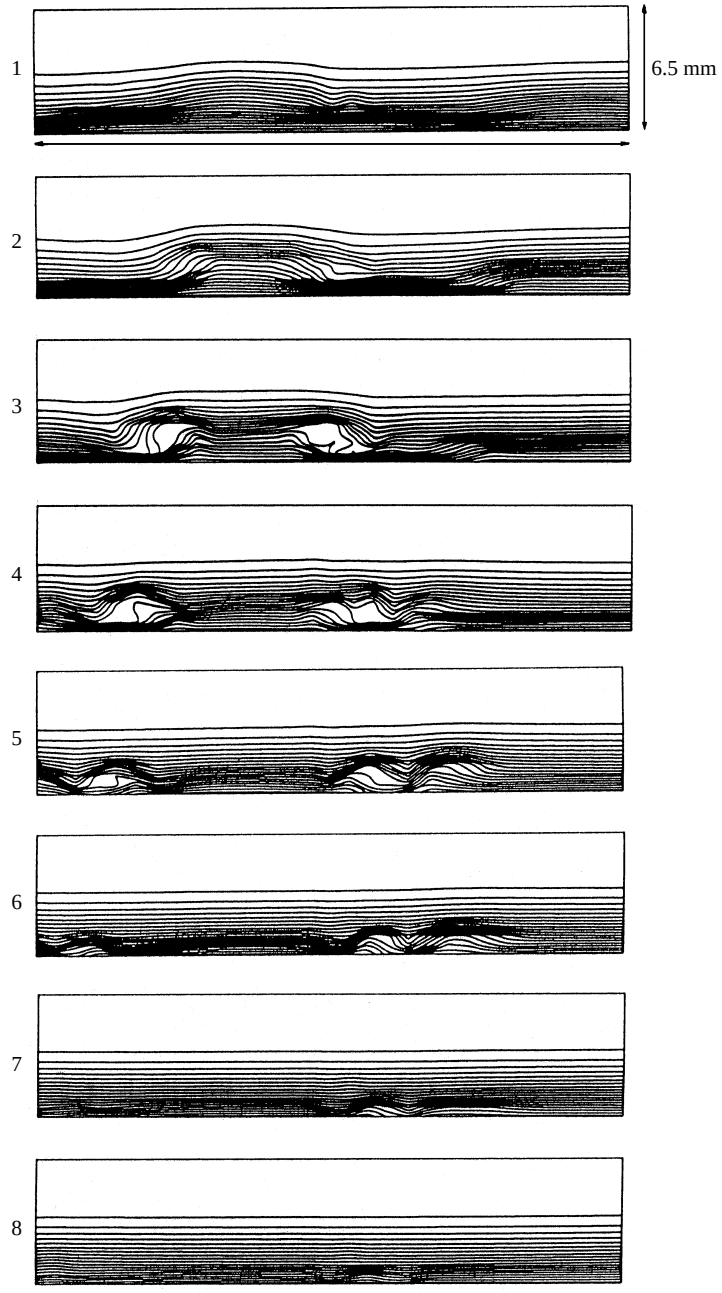

FIGURE 28. The development of total velocity measurements at a number of time instants during the nonlinear development of the wavepacket flow of Gaster (1993).

complementary adjacent positive regions; although the hot wire measured the streamwise component of velocity only, the measurements suggest that the structure is an inclined horseshoe vortex propagating in the flow direction.

Figure 27 shows a number of velocity profiles obtained from the current experiment and those presented by Gaster (1993) obtained during the nonlinear development of an artificially excited wavepacket in a boundary layer flow. The two sets of profiles are

remarkably similar in form. The development of the associated streamwise velocity contours in the spanwise plane at a number of time instants is given in figure 28. The figure clearly shows the development of two steep shear layers that intensity to form 'eyes' before moving apart and decaying to the undisturbed form. This pattern of behaviour was also observed in the current experiment although the regions of shear were somewhat weaker. It is clear that the pattern of behaviour during the nonlinear evolution of the respective wave systems is quite similar.

The generation of Λ-shaped structures with associated regions of steep shear was originally observed during the nonlinear development of harmonically excited flows; the subsequent development of these flows has been documented extensively, see Kachanov (1994). It appears therefore, that the generation of a horseshoe vortex structure is common to the nonlinear evolution of a number of transitional flows. However, the subsequent breakdown of the flow and the generation of chaotic disturbances appear to be quite different in the modulated and non-modulated cases. Whereas the latter flows are characterized by either the generation of multiple soliton-like spikes in the velocity records, or the rapid amplification of 'subharmonic' disturbances, both leading to the general randomization of the flow, modulated wave systems are characterized by a highly localized breakdown of the flow field and the formation of distinct turbulent spots resulting in flows with spatially evolving levels of intermittency. The investigation described in the following section was designed to examine the localized breakdown of modulated disturbances in greater detail.

6. Breakdown of an event

6.1. *Background and experimental parameters*

The free-stream velocity was set at 18 m s^{-1} for this experiment. An 8 kilobyte record of computer-generated white noise was used to excite the laminar boundary layer. Hot-wire measurements were made at 12 streamwise locations along the centreline of the plate, covering $0.243 \leqslant Re_{\delta^*} \times 10^{-3} \leqslant 1.516$, at six stations normal to the wall. The locations of the streamwise measurement stations are listed in table 2. The boundary layer was excited with the same noise sequence 40 times at each measurement station. The fluctuating component of the streamwise velocity was preamplified, passed through a 4–6000 Hz band-pass filter before being sampled at a rate of 12.5 kHz. A second channel digitized the total streamwise velocity signal at the same rate. In total 54 Mb of data was obtained during the course of the experiment.

General results obtained from this experiment using traditional signal processing techniques were described initially by Skaikh (1997) and a summary of the major findings was given in §1.2. The aim here is to use the WT to examine in detail the localized breakdown of the flow field and the generation of high-frequency disturbances. Some aspects of the this work were discussed briefly by Gaster (1993); a more detailed account focusing on localized breakdown and the initial generation of high-frequency disturbances is given here.

6.2. *Results*

A 1 kilobyte segment of time series centred about the eventual position of an event was extracted from each of the 40 times series obtained at each measurement station. The data were passed initially through a Hanning window and then analysed using the WT algorithm discussed in §2.2. The complex Morlet and modified Morlet wavelets with $m = 5.33$ were used in this analysis.

6.2.1. *Evolution of high-frequency disturbances*

The magnitude of the wavelet coefficients at 250 scales was calculated for each velocity record. This range of scales corresponded to a family of Fourier domain band-pass filters with centre frequencies in the range $60 \leqslant f \leqslant 6000$ Hz. Figure 29 shows the variation of the magnitude of the transform plane with increasing streamwise distance for a constant non-dimensional distance from the wall given by $\eta = 4.24$. This location is close to the edge of the boundary layer and the velocity records from this region of the flow do not contain evidence of the large-amplitude event observed in the signals from measurement stations nearer the wall. Although the examination of the velocity records indicated that the localized event first occurred in the lower region of the boundary layer, the development of the velocity fluctuations can be viewed more clearly from this outer position.

The figure shows four separate diagrams corresponding to positions 960, 965, 1000 and 1050 mm from the leading edge of the plate. Each individual diagram shows the section of time series that was analysed using the WT and a colour plot showing the magnitude of the calculated wavelet coefficients. The ordinate of both plots at each location is time, whilst the abscissa for the time series are normalized velocities. The abscissa of the colour plots is logarithmic in the scale parameter; however, the plots have been marked with two filter centre frequencies for clarity. The wavelet coefficients have been normalized by the maximum value at each measurement location and the key shows the distribution of the colour scale. The red and lighter colours correspond to a high value of the wavelet coefficient whilst the blue colours are associated with extremely low values.

Figure 29(*a*) indicates that the majority of the signal energy at this location is contained within two distinct frequency bands, $160 \leqslant f \leqslant 400$ Hz and $100 \leqslant f \leqslant 160$ Hz, corresponding to the T–S and subharmonic frequency ranges respectively. Moving downstream 5 mm, the velocity record in figure 29(*b*) shows the first indications of the development of higher-frequency oscillations. A close examination of the wavelet plane shows that the frequency of these fluctuations is centred on roughly 1 kHz.

At a distance 1000 mm from the leading edge, figure 29(*c*) indicates that the patch of high-frequency oscillations covers a greater proportion of the time series and contains a wider spectral range of frequencies. The final diagram, figure 29(*d*), corresponding to a location 50 mm further downstream, shows that the high-frequency oscillations are the only discernible feature of the time series at this scale: the T–S disturbances are still present but are of considerably smaller amplitude. The associated wavelet plane confirms this and indicates that the majority of the signal energy is still concentrated in a fairly narrow spectral band centred on a frequency of 1 kHz. A closer examination of the colour figure shows that there is also significant energy associated with an extremely narrow range of frequencies centred on 5 kHz.

The appearance and evolution of these higher-frequency disturbances are not as clear in the central and inner region of the boundary layer. Figure 30(*a*) shows time series and associated wavelet planes obtained at a distance 800 mm from the leading edge for two non-dimensional wall positions given by $\eta = 0.35$ and 1.1, corresponding to the inner and central regions of the boundary layer respectively. The colour coding used here is different to the previous figures: the distribution of the scales is identical but light green is now associated with large values of the wavelet coefficient and light red with lower values. The velocity signals clearly show a large-amplitude event that produces a wavelet plane dominated by low frequencies.

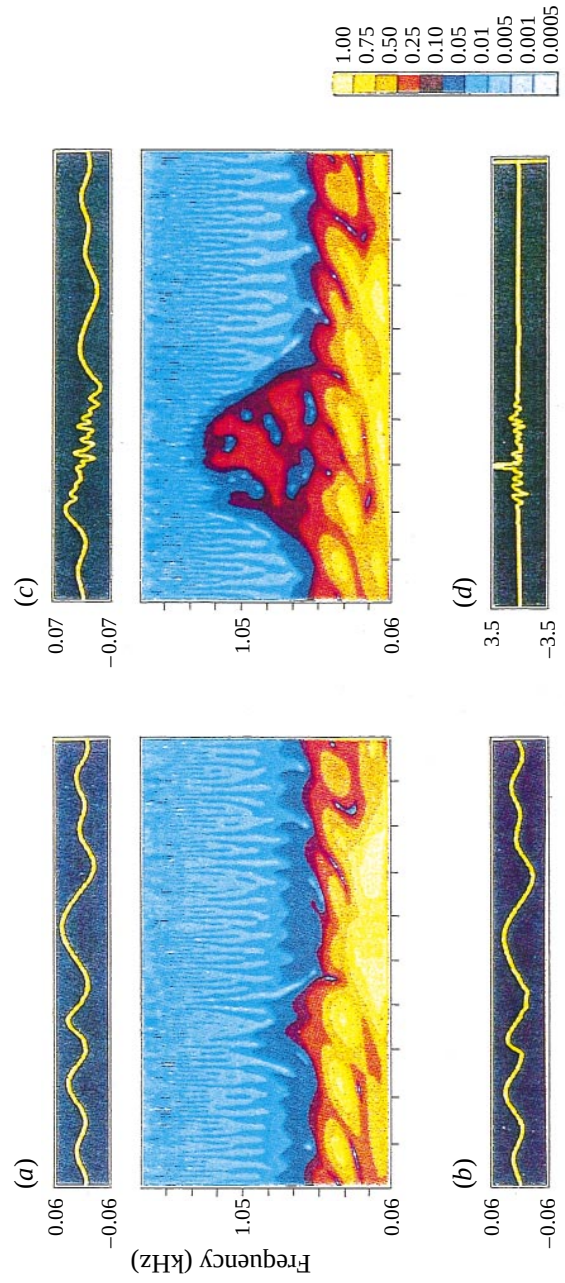

FIGURE 29. Original signal and wavelet transform modulus of fluctuating streamwise velocity signals from consecutive measurement stations at $\eta = 4.24$: (*a*) $x = 960$ mm; (*b*) $x = 965$ mm; (*c*) $x = 1000$ mm; (*d*) $x = 1050$ mm (using the Morlet wavelet).

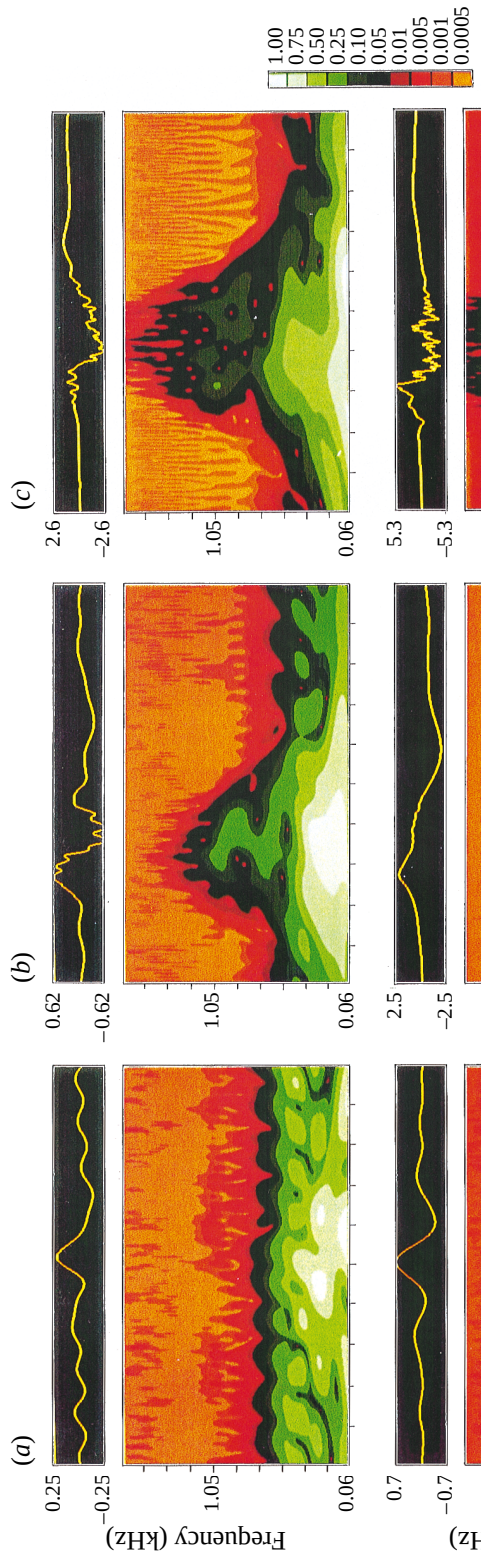

FIGURE 30. Original signal and wavelet transform modulus of fluctuating streamwise velocity signals at (*a*) $x = 800$ (*b*) $x = 1000$, (*c*) $x = 1050$ from $\eta = 0.35$ (top); $\eta = 1.1$ (bottom) (using the Morlet wavelet).

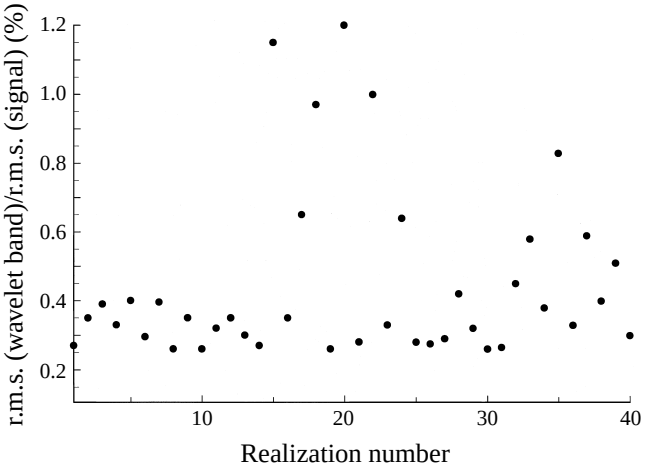

FIGURE 31. Variation of energy density in the frequency range $800 < f < 2000$ Hz calculated using the wavelet transform for 40 realizations obtained at $x = 975$ mm, $\eta = 4.24$ (using modified Morlet wavelet).

A further 200 mm downstream the time series in figure 30(*b*) exhibit high-frequency oscillations. The effect is more evident in the inner region of the boundary layer and, once again, these oscillations can be associated with a broad band of frequencies centred on a value of 1 kHz. Finally, figure 30(*c*) from a position 1050 mm from the leading edge shows that the time series have developed large-amplitude high-frequency oscillations. The wavelet plane associated with $\eta = 0.35$ indicates that the spectral range of these oscillations has broadened compared to the previous figure but is still centred around a value of 1 kHz. The diagram associated with $\eta = 1.1$, however, shows that the velocity record contains a wide spectral range of fluctuations at this location that is indicative of the passage of an nascent turbulent spot over the hot-wire probe.

The wavelet analysis of the velocity records suggests, therefore, that the localized event observed in the central region of the boundary layer developed bursts of high-frequency oscillations consisting initially of a narrow band of frequencies five or six times that of the fundamental T–S frequency. There was also some evidence of the development of another higher-frequency band of disturbances some twenty times that of the fundamental prior to the general broadening of the spectral distribution.

6.2.2. *Examination of intermittent behaviour*

The WT results suggested that the initial generation of the high-frequency bursts of oscillations in the velocity records was intermittent and appeared to be independent of the input forcing. The WT was used to detect the appearance of these oscillations by monitoring the energy density of the wavelet coefficients associated with the scales of the bursts. The wavelet plane associated with an event prior to the appearance of high frequencies will have very little energy associated with this region, whereas the energy density will increase during the breakdown process due to the increased disturbance amplitude as well as the broadening spectral content.

The 40 velocity records obtained at each measurement station were analysed using the WT and the energy density of the region given by $800 \leqslant f \leqslant 2000$ Hz was calculated for each realization. Figure 31 shows the variation of the energy density of this region of the wavelet plane for each realization obtained from the outermost measurement location at a position 975 mm from the leading edge. The figure indicates that the

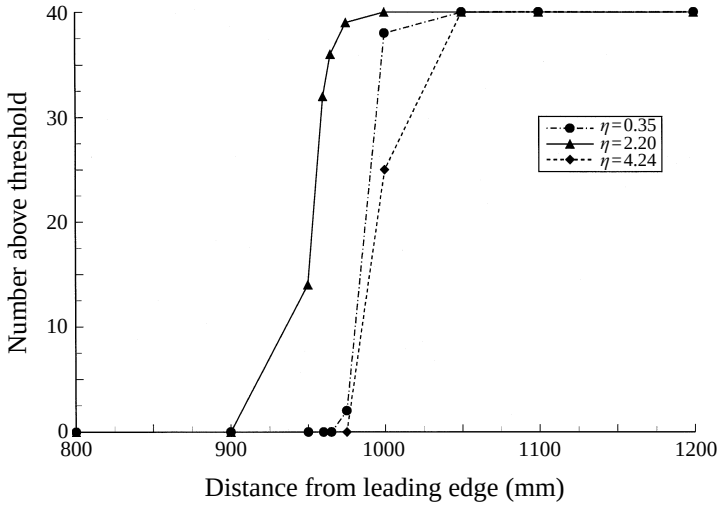

FIGURE 32. Variation with streamwise distance of the number of realizations above the wavelet modulus threshold criterion (in the pass band $800 < f < 2000$ Hz) for three distances from the wall (using modified Morlet wavelet).

majority of the velocity records have a similar energy density level of $\approx 0.3\,\%$, although a number do have values above this level. A section of the time series from one such realization is given in figure 4: a high-frequency burst of oscillations is clearly superimposed on the background signal.

The numerical value of the energy density is obviously dependent on the r.m.s. level of the velocity signal. This can vary by a factor of 30 through the boundary layer, and so an absolute energy density level was assigned by inspection as an indication of significant energy in the prescribed region of the wavelet plane. Figure 32 shows how the number of realizations above this threshold varies with streamwise distance for three non-dimensional boundary layer heights. The figure indicates that initially the high-frequency bursts occur intermittently in the central region of the boundary layer before being observed in the inner and outer regions.

The WT was also used to filter the velocity records in the time and frequency domains by selectively reconstructing a section of the transform plane. The wavelet used in the forward transform must satisfy an admissibility condition (2) and, in addition, the borders of the selected region must be parallel to the time and frequency domain zones of influence discussed in §2.2. The modified Morlet wavelet was used to reconstruct the region of the transform plane given by $800 \leqslant f \leqslant 2000$ Hz, and figure 33(*a–c*) show the results of this filtering process for a number of realizations obtained from the innermost measurement station at three streamwise locations. In general two structures can be seen, the first is the filtered remnant of the localized event and the second is the high-frequency burst of interest. A comparison of the figures indicates that in general, the number of realizations with high-frequency bursts and the amplitude of the bursts increase with streamwise distance.

6.3. *Discussion*

The wavelet analysis of an event suggested that prior to breakdown the signals were composed from disturbances with frequencies lower than those associated with the fundamental T–S waves. Further downstream a number of realizations from the central region of the boundary layer exhibited bursts of higher-frequency oscillations,

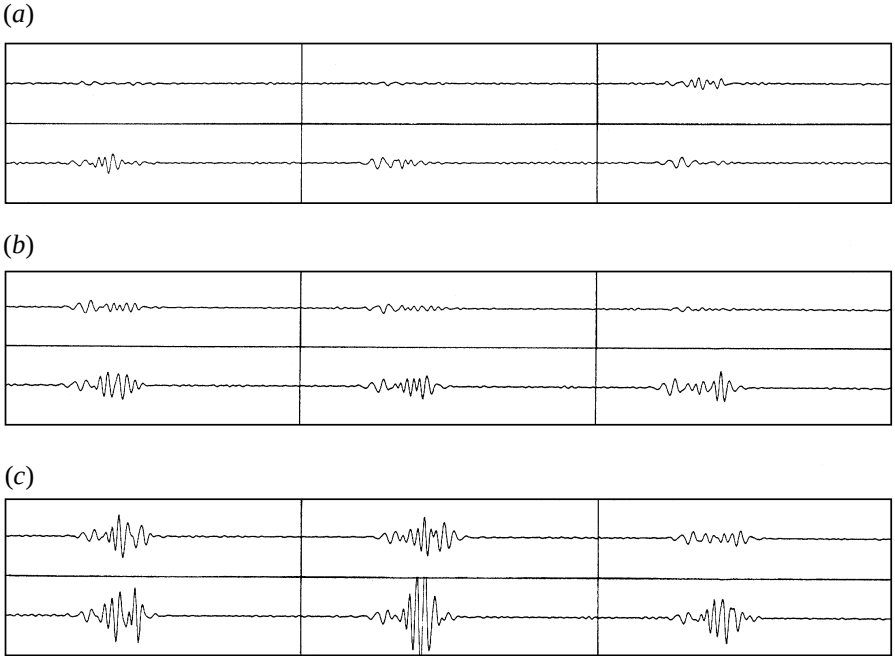

FIGURE 33. Reconstructed region of the transform plane given by $800 < f < 2000$ Hz for a number of realizations at $\eta = 0.35$ for consecutive measurement stations: (*a*) $x = 960$ mm; (*b*) $x = 965$ mm; (*c*) $x = 975$ mm (using the modified Morlet wavelet).

some five or six times that the basic instability waves. These disturbances initially had the form of a wavepacket of narrow spectral content that broadened with increasing streamwise distance. This behaviour was observed by Gaster (1978, 1993) during the nonlinear development of an artificially excited wavepacket. Both the current and wavepacket experiments were conducted at similar free-stream velocities but on different flat-plate models in different experimental facilities.

The wavelet filtered results showed that the bursts consisted of wavepacket structures with modulated envelopes that became less intermittent and grew in amplitude and time duration with increasing streamwise distance. There appeared to be no pattern to the appearance of these disturbances within the 40 realizations obtained at a single measurement station. It appears, therefore, that these bursts were not excited deterministically by the forcing white-noise signal.

Once formed the high-frequency oscillations developed rapidly with streamwise distance, growing in amplitude and broadening in spectral content. There was some evidence that the velocity records subsequently developed oscillations with a narrow band of frequencies some twenty times that of the fundamental instability waves. The relatively low sampling rate prevented further confirmation of the generation of this cascade of successively higher frequency disturbances leading to turbulence. However, Gaster (1978) observed a similar phenomenon in the wavepacket flow.

The wavelet analysis of velocity records from locations further downstream suggested that the signals contained localized bursts of high-frequency disturbances with a wide spectral content that was reminiscent of turbulent flow. These regions can be considered to be embryonic turbulent spots. It is interesting to note that in the current experiment, the entire process, from the first appearance of the high-frequency disturbances to the generation of turbulent patches in the flow, occurred over a

distance of approximately 50 mm, or one or two wavelengths of the fundamental T–S instability waves.

7. The final stage of transition to turbulence

7.1. *Background and experimental parameters*

Here computer-generated white-noise records were used once again to excite the laminar boundary layer. However, in these experiments excitation signals of varying amplitudes and phase dispositions between the spectral components were used to investigate spot propagation characteristics and the global properties of intermittent boundary layers.

The free-stream velocity was set at $17.5\ \mathrm{m\ s^{-1}}$ for these experiments. Three 32 kilobyte white-noise sequences were used to excite the boundary layer at four closely spaced normalized levels of excitation: 1.0, 1.04, 1.08 and 1.12 (levels 1–4). This small range of levels was chosen to ensure that the process of breakdown did not change radically through a different (bypass) process that would confuse the interpretation of the experiments. In addition, it was desirable to ensure that the excitation signals were sufficiently weak to allow the initial disturbance waves to grow linearly before becoming large enough for the breakdown process to occur. The three excitation sequences (A, B and C) had identical spectral content but had different randomized phase dispositions between the spectral components.

Initially, boundary layer traverses were made with the hot wire to ensure that the mean flow velocity profiles were appropriate to a zero-pressure-gradient Blasius form. The flow oscillations generated by a particular noise signal at a specific level of excitation were then mapped out in both space and time by repeatedly exciting the boundary layer with the sequence and measuring the response with a hot-wire probe positioned at different downstream stations.

The measurements presented here were obtained at a single non-dimensional height given by $\eta = 1.1$. Recordings of the hot-wire response were made at a number of streamwise stations in the range $800 \leqslant x \leqslant 1250$ mm ($1670 \leqslant Re_{\delta^*} \leqslant 2100$) in steps of 50 mm and at intervals of 20 mm across the span $-120 \leqslant z \leqslant 120$ mm. At each station 32 kilobyte of data were recorded at a sampling rate of 25 kHz. The unsteady signal from the hot-wire anemometer was preamplified and filtered in the range 4 Hz to 10 kHz before being sampled and stored. A second channel digitized the full anemometer signal at the same sampling rate. The recordings were repeated for the three noise sequences at the four levels of excitation, generating 50 Mb of data.

7.2. *Results*

7.2.1. *Typical velocity records*

Figure 17(*a–d*) shows velocity records obtained from four consecutive streamwise locations at a single spanwise position and are typical of the measured boundary layer response to the levels of excitation used. These signals are not averaged and correspond to 'single shot' recordings. The characteristics of these signals were discussed in §3.3 in the context of spot detection and tracking using SSA and are reviewed briefly here. Figure 17(*a*) from the most upstream location shows a signal containing violent excursions or events separated by regions of inactivity. Although the events differ from one another in their detail and amplitude, there is some similarity in the overall pattern. The results from §§5 and 6 suggest that the events are correlated through the boundary layer and mark the occurrence of a short period during which the velocity profiles are inflectional. The highly three-dimensional flow structures associated with these profiles

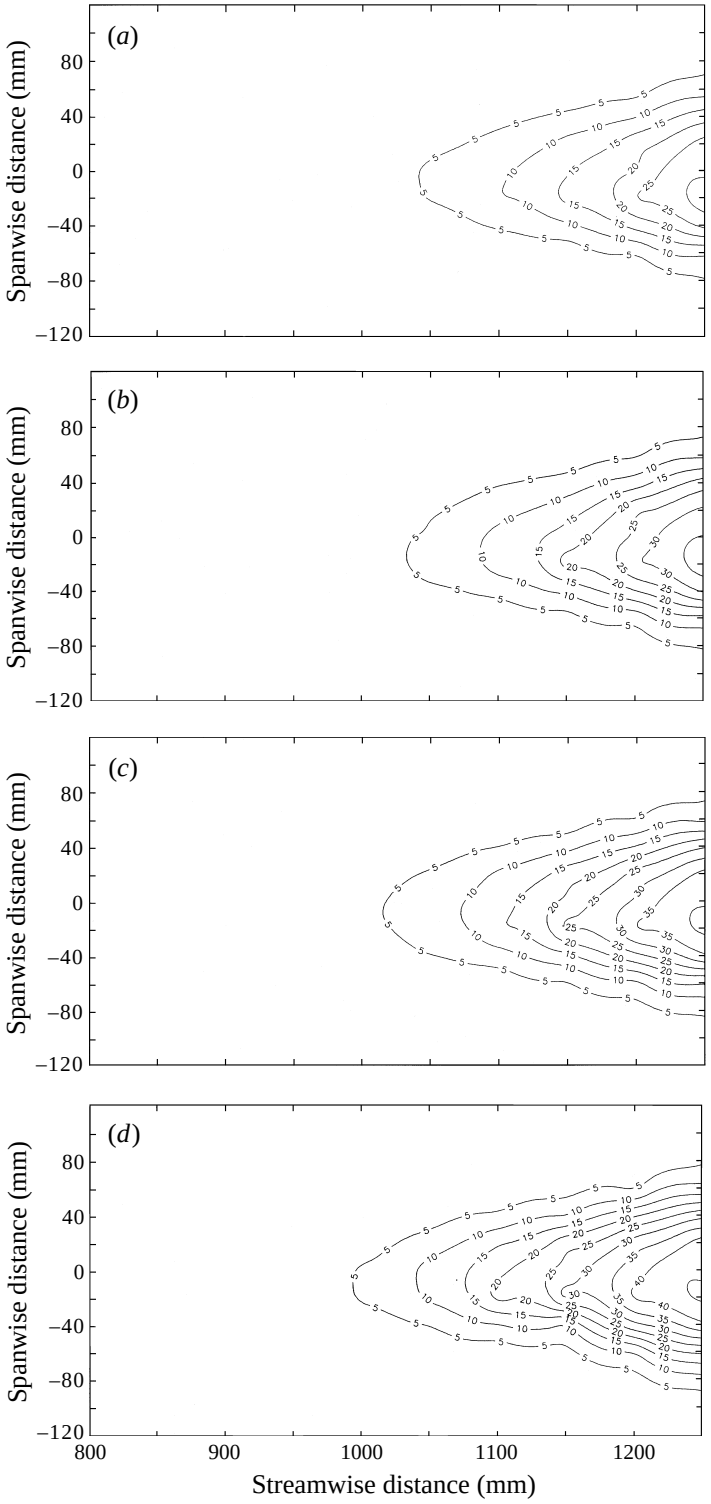

FIGURE 34. Contour plots of the calculated signal intermittency for excitation sequence A at (*a*) amplitude level 1, (*b*) level 2, (*c*) level 3, (*d*) level 4.

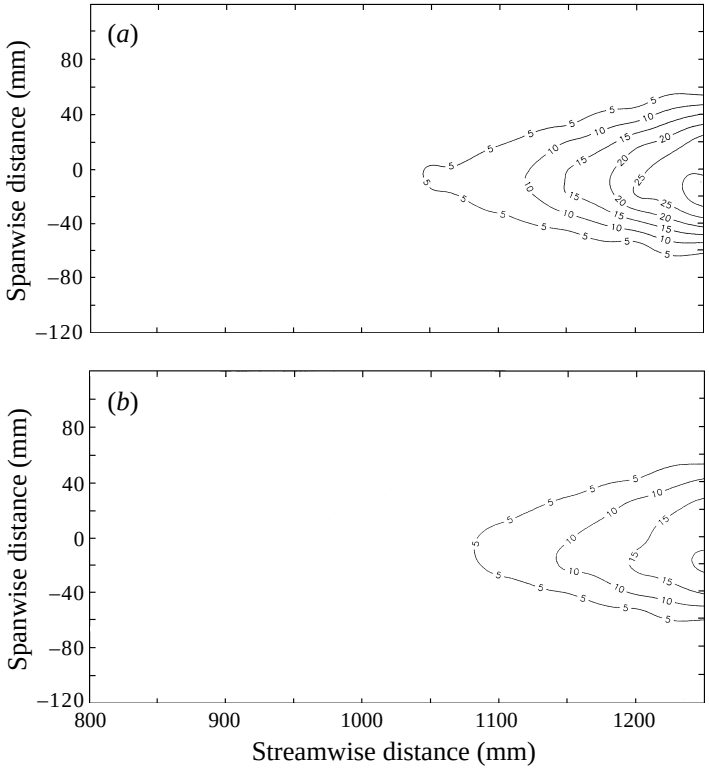

FIGURE 35. Contour plots of the calculated signal intermittency for (*a*) excitation sequence B and (*b*) sequence C, at amplitude level 3.

break down through a cascade of high-frequency disturbances and are the precursor to the formation of turbulent spots. In fact, spot 1, marked on figure 17(*a*) contains a high-frequency burst of oscillations superimposed on the signal. Although the regions between the events appear to be quiescent, they in fact contain highly modulated disturbance waves, albeit of very low relative amplitude.

The progress of the disturbance flow field with increasing downstream distance is shown in figure 17(*b–d*). The events in this signal appear at the same relative positions as those in figure 17(*a*) and show quite clearly that they are deterministic and controlled by the input excitation. The internal structure of the high-frequency disturbances may not be repeatable from realization to realization, but the position of the structures is determined by the input excitation. The amplitudes of the major excursions increase with streamwise distance and, in addition, previously smooth events show high-frequency oscillations, marking the locations of turbulent spots. New events have also appeared from regions of the signal that were dormant at the upstream location.

7.2.2. *Intermittency measurements*

The spot detection technique described in § 3.3 was used to calculate the intermittency of the boundary layer flow from the measured hot-wire data. Shaikh & Gaster (1993, 1994*b*) briefly presented a number of results from this investigation, a more detailed and cohesive discussion is given here.

Figure 34(*a–d*) shows plan view contour plots of the calculated intermittency for excitation sequence A at the four levels of excitation respectively. The series of figures

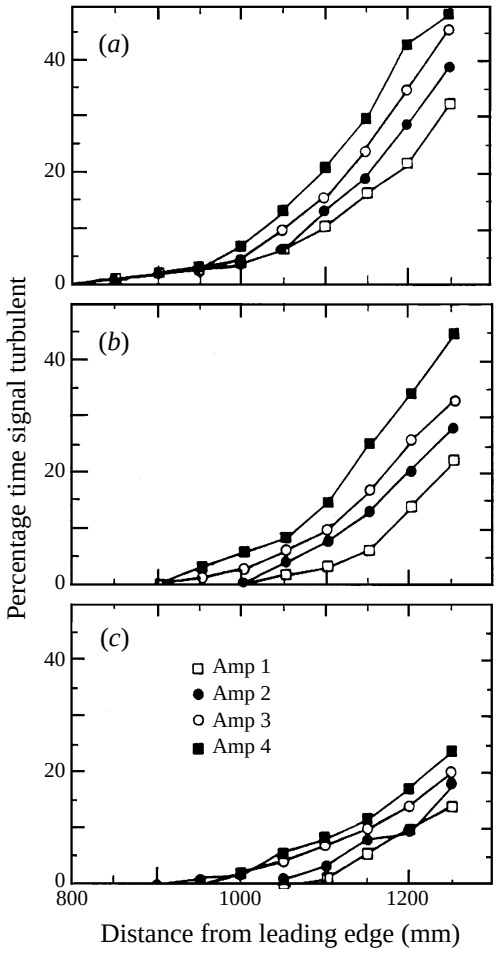

FIGURE 36. Centreline intermittency distributions at four amplitude levels for: (*a*) sequence A; (*b*) sequence B; (*c*) sequence C.

shows the region swept out by the spots generated by the signal from the point source on the centreline. At the lowest amplitude of excitation, spots first occurred approximately 1 m downstream of the leading edge ($Re_{\delta^*} = 1870$). The contour pattern shows a slight asymmetry, presumably because the boundary layer was not precisely two-dimensional at extreme distances from the leading edge. Figure 34(*b–d*) shows how this intermittency pattern developed with increasing levels of excitation. As perhaps might have been anticipated, the wedge of disturbances moves upstream and the growth of intermittency is more rapid at the large excitation amplitudes. Each velocity record corresponded to a sampled time of 1.3 s or 260 T–S wave periods; clearly, a much longer duration of time series is required in order to form statistically representative estimates of the intermittency.

Figures 35(*a*, *b*) shows similar plots arising from white-noise sequences B and C at amplitude 3 respectively. A comparison of these figures with that due to series A, amplitude 3 (figure 34*c*) show considerable differences: the intermittency distributions appear to have been produced by excitation of considerably differing amplitudes.

Figure 36(*a–c*) shows the form of the intermittency distributions in grater detail. Figure 36(*a*) shows the spatial growth of flow intermittency along the centreline at the

four excitation levels for case A. The figure indicates that the streamwise development of the calculated intermittency is independent of excitation amplitudes for values less than 5%. Above this threshold the intermittency appears to grow exponentially, the rate dependent on the amplitude of excitation. Figure 36(*b*), on the other hand, shows the development of centreline intermittency for sequence B and indicates that the behaviour of the intermittency distributions is quite different from that of case A below the threshold of 5%. Here the location of the origin of the distributions appears to be dependent on the excitation amplitude, a larger value of the excitation tending to shift the origin of the disturbances upstream. However, the intermittency distributions behave in a manner similar to those in the previous figure at values greater than 5%, although the absolute magnitudes are somewhat lower.

The intermittency distributions generated by sequence C given in figure 36(*c*) that in this case the intermittency distributions grow at a comparatively lower rate: the maximum intermittency value is less half that associated with case-A. In addition, the positions of the origins of the distributions are again dependent on the magnitude of excitation.

There appears to be a difference in the early development of the intermittency distributions. Whereas increasing the excitation amplitude tended to shift the origin of the distributions upstream for sequences B and C, the distributions associated with sequence A appeared to be independent of the level of excitation. This discrepancy in behaviour could have arisen from the fact that the excitation levels covered a very small range and that the flow field was sampled coarsely in the streamwise direction. A large range of excitation levels would have probably resulted in a behaviour similar to that of sequences B and C.

There are a number of possible explanations for the difference in the intermittency growth rates below and above the threshold value of 5%. The most obvious is that the calculation method was not accurate for low levels of intermittency. However, the technique was tested on a range of signals and was found to be accurate even at low levels of the intermittency parameter.

Another explanation is that the method detected the high-frequency oscillations associated with the breakdown of the laminar flow to incipient turbulent spots in addition to those associated with more mature spots. Thus at low intermittency levels the flow field and the intermittency distributions were likely to be dominated by the dynamics of incipient turbulent spots, whereas at higher levels the distributions were dominated by the dynamics of more mature spots. In addition, the relatively coarse distribution of streamwise measurement stations may have resulted in an apparent abrupt change in the behaviour of the intermittency at the threshold value for sequences A and B, whereas the slow growth observed with sequence C permitted the change in behaviour to occur over a number of measurement stations and hence more smoothly.

Narasimha (1985) formulated an expression based on queuing theory for the intermittency distribution of a transitional two-dimensional flat-plate boundary layer. Although only strictly applicable to entirely two-dimensional flows, it may still be valid for the centreline intermittency distributions. The formulation assumed that spot generation and propagation could be described as a non-stationary Poisson stream in the space spanned by the streamwise, spanwise and time coordinates. The derivation was based on the following assumptions: the dynamics of a spot is independent of that of other spots; the spots form at a preferred streamwise location, x_t, randomly in time

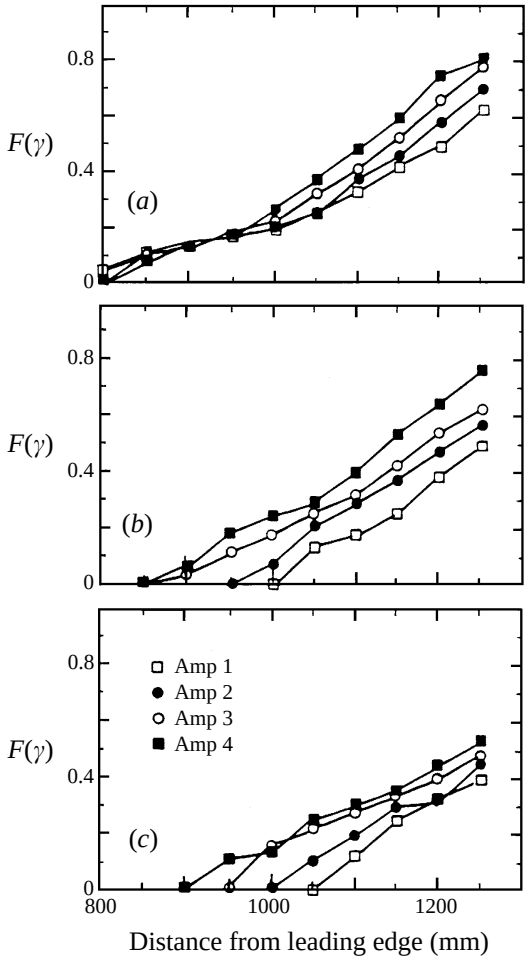

FIGURE 37. Centreline $F(\gamma)$ distributions at four amplitude levels for: (*a*) sequence A; (*b*) sequence B; (*c*) sequence C.

and the spanwise direction; the probability that two or more spots form near the same place and time is small. The resultant expression for the intermittency, γ, is given by

$$\gamma = 1 - \exp[A(x - x_t)^2],$$

where A is a constant. The position x_t is evaluated by finding the zero of the function

$$F(\gamma) = [-\ln(1-\gamma)]^{1/2}.$$

Figure 37(*a–c*) shows the variation of this function with streamwise distance for the three cases. The figures indicate that the intermittency does in fact vary exponentially with streamwise distance for large values of the parameter and imply that the above assumptions are valid for this region of the flow field.

7.2.3. *Spot dynamics*

The spot tracking technique described in §3.3 was used to follow the general development of correlated turbulent patches in the flow field. Although the correlated velocity records were obtained on a single-shot basis, the development of the correlated patches was surprisingly coherent and provided useful information on the general evolution of individual turbulent spots.

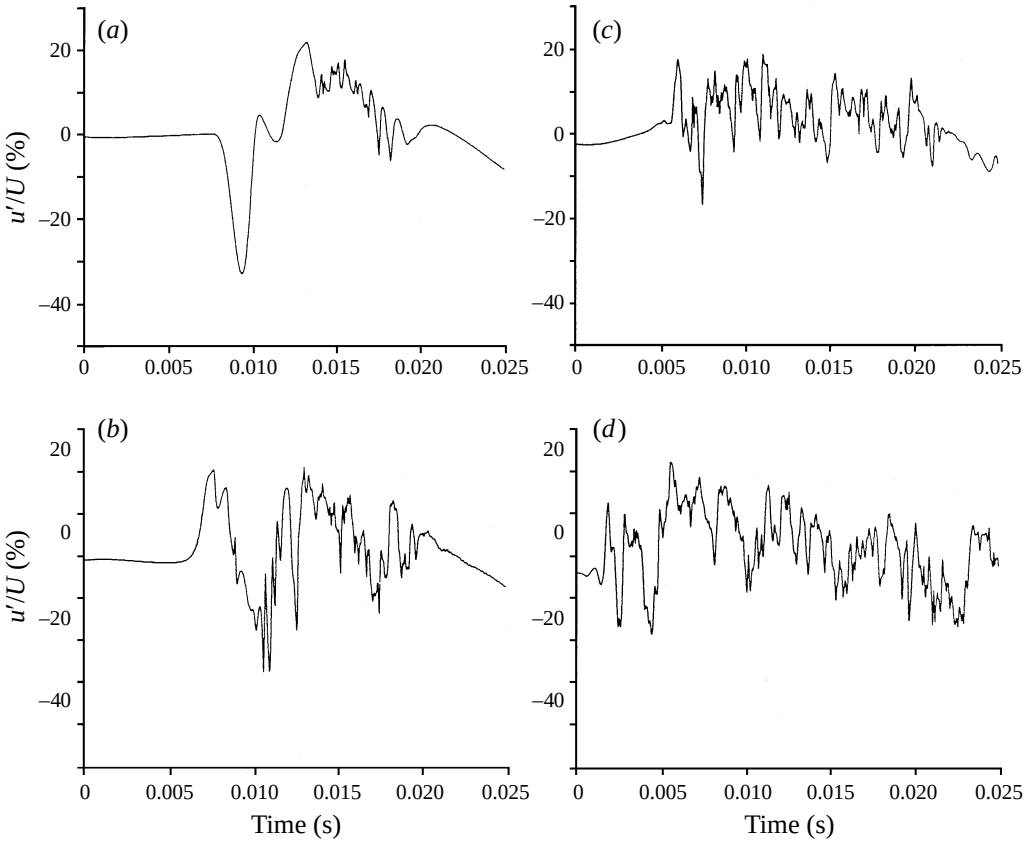

FIGURE 38. Incipient spot development, $z = 0.02$ m: (*a*) $x = 1.1$ m; (*b*) $x = 1.15$ m; (*c*) $x = 1.2$ m; (*d*) $x = 1.25$ m.

The detection technique permitted the propagation characteristics of individual spots to be studied by charting the streamwise development of the temporal extent of the high-frequency oscillations in the velocity records. Measurements from large turbulent patches indicated that the spot interfaces propagated at constant velocities, the spot leading edge travelling at $0.90U_0$ and the trailing edge at $0.48U_0$. These values compare well with the measurements of Schubauer & Klebanoff (1955) who reported values of $0.88U_0$ and $0.50U_0$ respectively. However, measurements of smaller patches immediately following inception indicated that the temporal extent of these structures grew at slightly faster rates.

Figure 38(*a–d*) shows time series extracted from a single coherent spot at a number of consecutive streamwise locations and correspond to snapshots of typical flow structures that appear during the evolution of a spot. Figure 38(*a*) shows a signal containing a large-amplitude event immediately after the breakdown of the flow and the appearance of high-frequency disturbances. This region of the flow field broadens in figure 38(*b*) some 50 mm further downstream and develops disturbances with a wide range of frequencies in figure 38(*c*). The final figure, figure 38(*d*), shows what appears to be a fully turbulent spot.

The wavelet transform was used to give a more detailed description of the spot development in terms of both frequency content and temporal extent. The signals shown in figure 38(*a–c*) were analysed using the wavelet transform and the resulting

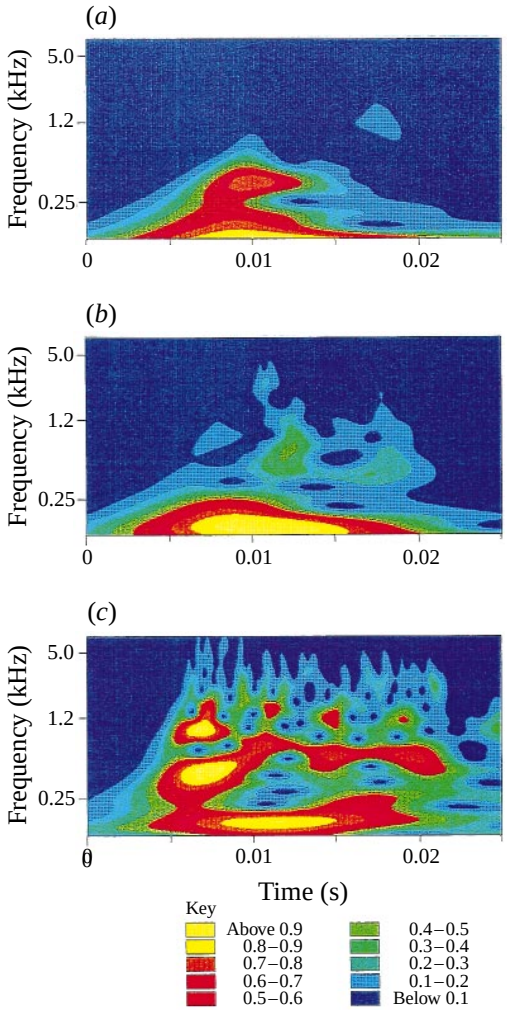

Figure 39

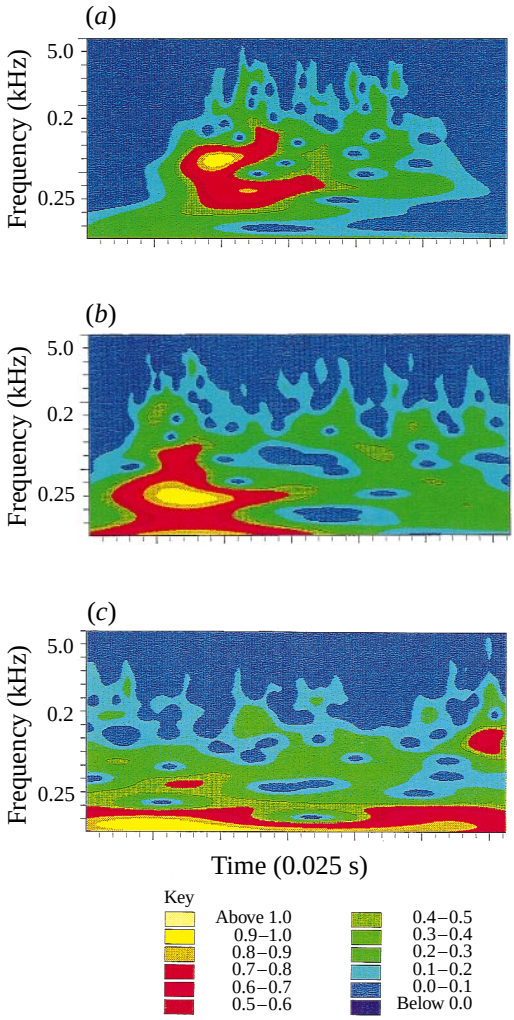

Figure 40 (*a–c*)

FIGURE 39. The evolution of a turbulent spot described in terms of the wavelet plane at three streamwise locations using the modified Morlet wavelet: (*a*) $x = 1.1$ m; (*b*) $x = 1.15$ m; (*c*) $x = 1.2$ m (see figure 38).

FIGURE 40(*a–c*). For caption see facing page.

wavelet planes are given in figure 39(*a–c*). Figure 39(*a*) indicates that the previously noted burst of oscillations has a frequency approximately five times that of the fundamental T–S disturbances. The following diagram, figure 39(*b*), shows that the region of the signal containing these higher-frequency oscillations has developed to cover a greater proportion of the velocity record and shows a significant increase in bandwidth, although not sufficiently wide to indicate the appearance of fully turbulent flow. In addition, there is some evidence of signal energy in a frequency approximately twenty times that of the fundamental. Thus the flow structure associated with this signal does not correspond to a mature turbulent spot but to an intermediate structure. Figure 39(*c*) shows that signal given in figure 38(*c*) contains a wide range of frequencies but has significant coherence in the wavelet plane. The wavelet plane shows a well-organized structure, and there appears to be residual signal energy in the low

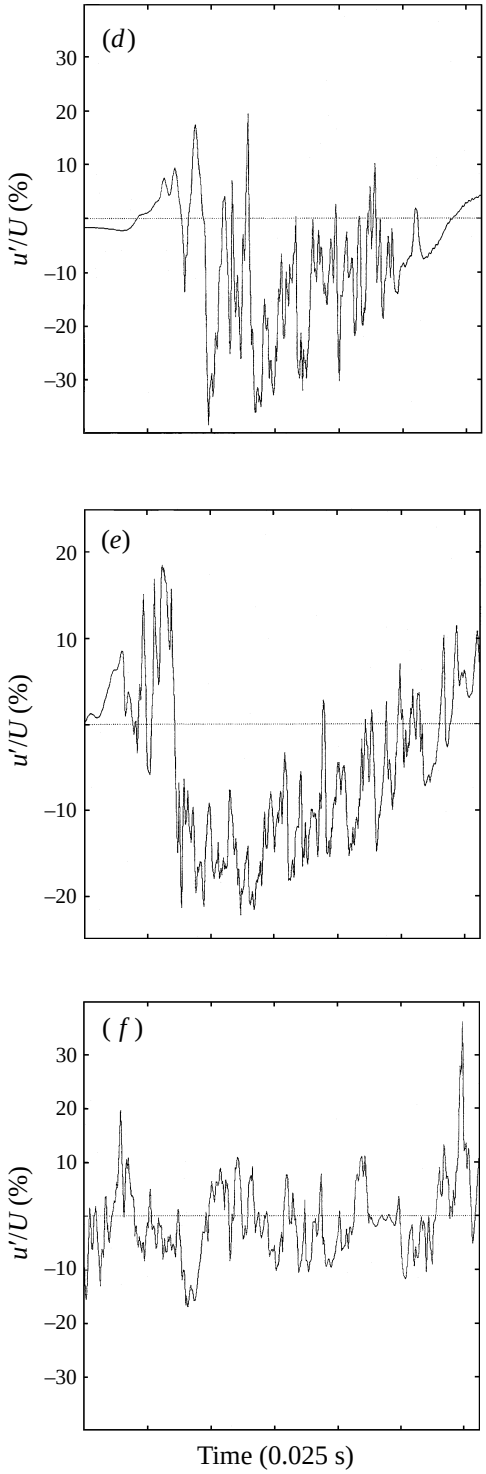

FIGURE 40. (*a–c*) Wavelet plane and (*d–f*) associated time series of (*a*, *d*) a nascent turbulent spot; (*b*, *e*) an older nascent turbulent spot; (*c*, *f*) a turbulent spot.

frequencies that is linked to the original large-amplitude event. In addition, the leading edge of the structure shows two localized concentrations of energy in the T–S and five times the T–S frequency ranges; it is reasonable to assume that these correspond to coherent structures within the body of the nascent spot.

The evolution of nascent spots can be seen more clearly in figure 40(*a–c*), which shows the wavelet planes of three separate flow structures of increasing 'age' or temporal extent given in figure 40(*d–f*). The wavelet plane in figure 40(*a*), associated with the youngest structure, once again shows a coherent region at the leading edge of the nascent spot with significant energy in the T–S and five times the T–S frequency ranges. This feature is also apparent in the wavelet plane given in figure 40(*b*) corresponding to the older flow structure, although the remainder of the signal shows less coherence and contains a broad range of frequencies. finally, the wavelet plane associated with the oldest flow structure given in figure 40(*c*) contains a broad range of frequencies with little coherence compared with the previous figures. It appears therefore, that following the breakdown of an event, a nascent spot requires a finite spatial distance in which to develop the broad spectral characteristics normally associated with mature turbulent spots.

7.3. *Discussion*

Although very much longer time series are necessary to form statistically representative estimates of intermittency and spot generation distributions, the white-noise experiments showed a number of interesting features. The three noise sequences used had identical spectral content but had different randomized phase dispositions between the spectral components. As would be expected for the small range of amplitude levels used, an increase in the excitation amplitude resulted in spots forming at more upstream locations; however, the cumulative spot distribution appeared to be independent of the excitation. Thus the location and initial formation of spots was dependent on the form and amplitude of the initial excitation, whereas the subsequent propagation characteristics were not.

It is interesting to note that the three sequences generated significantly different intermittency and spot generation distributions. Spots formed at different spatial locations within the flow field for the three different sequences. This implies that the phase dispositions between the spectral components of the excitation sequences played an important role in fixing the spatio-temporal location of an event in the flow field and hence determined the eventual location of turbulent spots. The flow intermittency varied exponentially with streamwise distance for large values of the parameter suggesting that the assumptions of the Narasimha (1985) model were valid for this region of the flow field even for short samples.

The pattern of high-frequency generation noted during the breakdown of a single event in §6 was also observed in the current experiments. The initial stage of breakdown was characterized by a cascade of successively higher-frequency disturbances that occurred over a small spatial distance. This lead to a degree of flow randomization and the inception stage of spot development. The flow at this stage retained some features of the previous flow and was characterized by a wider bandwidth of disturbances superimposed on the original cascade. The leading edge of the flow structure showed evidence of coherent regions that decayed as the nascent spot continued to evolve. The following stage is marked by a growth in the spatial extent of the flow structures and a progressive broadening of the spectral content. This development takes place over a spatial distance comparable to a T–S wavelength and leads eventually to the formation of a mature spot. The propagation characteristics of these spots agree with the results from previous investigations that used very much larger spots.

8. Conclusions

Previous experiments have suggested that the nonlinear evolution and subsequent breakdown of amplitude-modulated wavetrains is somewhat different to that of purely harmonic wave systems. Modulated disturbances are generally observed in both flight and naturally excited wind tunnel experiments and thus the differing routes to turbulence warrant further study. This investigation used sequences of computer-generated deterministic white noise to excite a laminar boundary layer via an embedded loudspeaker in a flat-plate model. This form of excitation generates the modulated disturbances of interest a short distance downstream of the source. By repeatedly exciting the boundary layer with the same noise sequence, it is possible to examine the subsequent evolution of the modulated disturbance system in a controlled manner with a single hot-wire probe.

Preliminary experiments indicated that the pattern of evolution of the artificially excited system was quantitatively similar to that observed in the naturally excited situation. The modulated waves initially pass through a stage of linear growth in which certain spectral components of the disturbance system grow in magnitude with downstream distance. The subsequent nonlinear stage is characterized by localized deviations from the linear pattern at isolated time instants. These isolated 'events' in the hot-wire records grow rapidly in magnitude compared to the remainder of the record. The third stage in the evolution of the flow field is marked by the localized breakdown of the events and the formation of embryonic turbulent spots. Global Fourier techniques were unable to resolve the localized nature of the velocity records from these highly nonlinear regions of the flow field; thus two local analysis techniques, the wavelet transform (WT) and singular spectrum analysis (SSA), were used to characterize these regions of the flow.

The results from three experiments that used the white-noise technique to examine the localized breakdown of the flow field are presented here. The first experiment mapped out the three-dimensional flow structure associated with the development of an event in the hot-wire records prior to the breakdown of the flow. The second examined the breakdown process itself, whilst the third investigated the subsequent development of the localized flow structures and the formation of turbulent spots.

The events were found to be linked to a highly three-dimensional flow structure propagating in the boundary layer flow. The central region of the structure was characterized by the rapid development of highly inflectional velocity profiles and associated regions of high shear followed by a 'calmed' region. The overall form of this structure resembled an inclined horseshoe vortex propagating in the flow direction. There is some evidence to suggest that unsteady inviscid three-dimensional asymptotic methods may go some way to describing the mechanisms driving the development of this structure.

Similar structures have been observed previously in harmonically excited and wavepacket flows. However, the subsequent development of the modulated disturbance systems appear to be somewhat different to that of the harmonically excited flows. The breakdown of the modulated wave systems is characterized by the generation of a cascade of successively higher-frequency disturbances. Two disturbance frequency ranges, some five (range I) times and twenty (range II) times that of the basic T–S frequency have been identified here. These values match exactly those reported by Gaster (1978, 1993) during the breakdown of a wavepacket flow. Gaster (1978) linked range I to the inviscid instability of the instantaneous inflectional velocity profiles identified in the flow and suggested that range II was generated by a further instability

resulting from the 'crinkling' of the velocity profile. Both the original wavepacket work and the current experiments were conducted in approximately similar boundary layers at similar free-stream velocities; thus it is reasonable to speculate that an inviscid breakdown is triggered when the instantaneous velocity profiles attain some characteristic saturated state.

Following breakdown, the flow structure develops a wider spectral range of disturbances but still retains some characteristics of the previous flow. There is some evidence to suggest that the leading edge contains a coherent region with the same two-tier cascade structure that may be the main mechanism for growth and would account for the faster spot growth rates observed immediately after inception. At this stage the flow structures do not exhibit the wide range of frequencies normally associated with turbulent flow and hence can be termed a nascent spot. The final stage of spot development is characterized by the generation of a progressively wider spectral range of disturbances. The propagation characteristics of these structures and the development of the flow intermittency from this region of the flow field compared well with measurements from previous investigations.

The author wishes to express his gratitude to Professor M. Gaster for his invaluable advice, help and guidance during the course of this work and additionally thanks the Engineering and Physical Sciences Research Council for financial support.

REFERENCES

Bergé, P., Pomeau, Y. & Vidal, C. 1994 *Order within Chaos*. John Wiley and Sons.

Broomhead, D. S. & King, G. P. 1986 Extracting qualitative dynamics from experimental data. *Physica* D, **20**, 217–236.

Combes, J. M., Grossman, A. & Tchamitchian, P. 1989 *Wavelets Time-Frequency Methods and Phase Space*. Springer.

Doorly, D. J. & Smith, F. T. 1992 Initial-value problems for spot disturbances in incompressible or compressible boundary layers. *J. Engng Maths* **26**, 87–106.

Farge, M. 1992 Wavelet transforms and their application to turbulence. *Ann. Rev. Fluid Mech.* **24**, 395–457.

Gabor, D. 1946 Theory of communication. *J. Inst. Elec. Engrs* **93**, 429–457.

Gaster, M. 1978 The physical processes causing breakdown to turbulence. In *12th Naval Hydrodynamics Symp, Washington DC*.

Gaster, M. 1981 On the transition to turbulence in boundary layers. In *Transition and Turbulence* (ed. R. E. Meyer). Academic.

Gaster, M. 1990 The non-linear phase of wave growth leading to chaos and breakdown to Turbulence as an example of an open system. *Proc. R. Soc. Lond.* A **430**, 3–24.

Gaster, M. 1993 The origins of turbulence. *Proc. Conf. on New Approaches and Concepts in Turbulence, Switzerland*. Birkhauser Basel.

Gaster, M. & Grant, I. 1975 An experimental investigation of the formation and development of a wave packet in a laminar boundary layer. *Proc. R. Soc. Lond.* A **347**, 253–269.

Kachanov, Yu. 1994 Physical mechanisms of laminar-boundary-layer transition. *Ann. Rev. Fluid Mech.* **26**, 411–482.

Kendall, J. M. 1985 Experimental study of disturbances produced in pre-transitional laminar boundary layer by weak freestream turbulence. *AIAA Paper* 85–1695.

Kendall, J. M. 1990 Boundary layer receptivity to weak freestream turbulence. *AIAA Paper* 89–1504.

Mullender, A. J. & Poll, D. I. A. 1995 Aircraft drag reduction, the application of natural laminar flow to aero-engine nacelles. In *Proc 12th ISADE, Melbourne, Australia*.

Narasimha, R. 1985 The laminar-turbulent transition zone in the boundary layer. *Prog. Aero. Sci.* **22**, 29–80.

PACKARD, N. H., CRUTCHFIELD, J. P., FARMER, J. D. & SHAW, R. S. 1980 Geometry from a time series. *Phys. Rev. Lett.* **45**, 712–716.

RIOUL, O. & FLANDRIN, P. 1992 Time-scale energy distributions: a general class extending wavelet transforms. *IEEE Trans. Signal Processing* **40**, 1746–1757.

SCHUBAUER, G. B. & KLEBANOFF, P. S. 1955 Contributions on the mechanics of boundary layer transition. *NACA Tech. Note* 3489.

SCHUBAUER, G. B. & SKRAMSTAD, H. K. 1948 Laminar boundary layer oscillations and transition on a flat plate. *NACA Tech. Rep.* 909 (Originally issued in 1943 as *NACA ACR.*).

SHAIKH, F. N. 1997 The generation of turbulent spots in a laminar boundary layer. To appear in *Eur. J. Mech.* B/*Fluids*, **16**, no. 2.

SHAIKH, F. N. & GASTER, M. 1993 The nonlinear evolution of modulated waves in a boundary layer. In *Proc. IUTAM Symp. on Nonlinear Instability of Nonparallel Flows*, *Potsdam*, *New York*, *USA*, *July 26th–31st*, pp. 147–159.

SHAIKH, F. N. & GASTER, M. 1994*a* The natural evolution of turbulent spots in a flat plate laminar boundary layer. In *Proc. IUTAM Symp. on Laminar-Turbulent Transition*, *Sendai*, *Japan*, *September 5–9*, pp. 271–278.

SHAIKH, F. N. & GASTER, M. 1994*b* The nonlinear evolution of modulated waves in a boundary layer. *J. Engng Maths* **28**, 55–71.

SMITH, F. T., DODIA, B. T. & BOWLES, R. G. A. 1994 On global and internal dynamics of spots: a theoretical approach. *J. Engng Maths* **28**, 73–91.

TAKENS, F. 1981 Detecting strange attractors in turbulence. In Lecture Notes in Mathematics, vol. 898 (ed. D. A. Rand & L. S. Young) Springer.

VAUTARD, R., YIOU, P. & GHIL, M. 1992 Singular-spectrum analysis: A toolkit for short, noisy chaotic signals. *Physica* D, **58**, 95–126.

WESTIN, K. J. A., BOIKO, A. V., KLINGMANN, B. G. B., KOZLOV, V. V. & ALFREDSSON, P. H. 1995 Experiments in a boundary layer subjected to free stream turbulence. Part 1. Boundary layer structure and receptivity. *J. Fluid Mech.* **281**, 193–218.